

AD \_\_\_\_\_

GRANT NUMBER DAMD17-94-J-4055

TITLE: Direct Digital Mammography Using Capillary Optics

PRINCIPAL INVESTIGATOR: Carolyn A. MacDonald, Ph.D.

CONTRACTING ORGANIZATION: New York State University at Albany  
Albany, New York 12201-0009

REPORT DATE: September 1998

TYPE OF REPORT: Annual

PREPARED FOR: Commander  
U.S. Army Medical Research and Materiel Command  
Fort Detrick, Frederick, Maryland 21702-5012

DISTRIBUTION STATEMENT: Approved for public release;  
distribution unlimited

The views, opinions and/or findings contained in this report are those of the author(s) and should not be construed as an official Department of the Army position, policy or decision unless so designated by other documentation.

19990820 010

# REPORT DOCUMENTATION PAGE

Form Approved  
OMB No. 0704-0188

Public reporting burden for this collection of information is estimated to average 1 hour per response, including the time for reviewing instructions, searching existing data sources, gathering and maintaining the data needed, and completing and reviewing the collection of information. Send comments regarding this burden estimate or any other aspect of this collection of information, including suggestions for reducing this burden, to Washington Headquarters Services, Directorate for Information Operations and Reports, 1215 Jefferson Davis Highway, Suite 1204, Arlington, VA 22202-4302, and to the Office of Management and Budget, Paperwork Reduction Project (0704-0188), Washington, DC 20503.

1. AGENCY USE ONLY (Leave blank)		2. REPORT DATE September 1998	3. REPORT TYPE AND DATES COVERED Annual (1 Sep 97 - 31 Aug 98)	
4. TITLE AND SUBTITLE Direct Digital Mammography Using Capillary Optics			5. FUNDING NUMBERS DAMD17-94-J-4055	
6. AUTHOR(S) Carolyn A. MacDonald, Ph.D.				
7. PERFORMING ORGANIZATION NAME(S) AND ADDRESS(ES) New York State University at Albany Albany, New York 12201-0009			8. PERFORMING ORGANIZATION REPORT NUMBER	
9. SPONSORING/MONITORING AGENCY NAME(S) AND ADDRESS(ES) Commander U.S. Army Medical Research and Materiel Command Fort Detrick, MD 21702-5012			10. SPONSORING/MONITORING AGENCY REPORT NUMBER	
11. SUPPLEMENTARY NOTES				
19990820 010				
12a. DISTRIBUTION / AVAILABILITY STATEMENT Approved for public release; distribution unlimited			12b. DISTRIBUTION CODE	
13. ABSTRACT (Maximum 200) The overall objective of this proposal is to develop a mammographic system with extremely high scatter rejection and dynamic range, good resolution and low patient dose. This will be accomplished by developing a direct x-ray detector interfaced with a capillary x-ray optic. Capillary x-ray optics, invented in the mid-eighties, provide an innovative new way to control x-ray beams. A number of promising geometries are being studied: collimating optics with long and short focal lengths, with and without antiscatter optics, monolithic linear magnifying tapers, and monolithic focusing, demagnifying optics. The collimating optics have transmissions in excess of 30% at their design energies, with collection angles ranging from 8 to 12 degrees. Scatter rejection is very high from all the optics. The linear tapers resulted in nearly ideal contrast enhancements and simultaneously increase in MTF at all spatial frequencies. The rapidly growing modeling capability is already leading to improvements in the manufacturing processes. Direct digital detectors owe their high efficiency and resolution to the direct detection of x-ray photons without requiring phosphors for the conversion to visible light. One dimensional "imaging" was demonstrated with the CZT linear array. CID two-dimensional arrays with small pixel sizes are another promising new technology for mammography.				
14. SUBJECT TERMS Mammography, Digital Mammography, Early Detection, Capillary X-Ray Optics, Breast Cancer			15. NUMBER OF PAGES 50	
			16. PRICE CODE	
17. SECURITY CLASSIFICATION OF REPORT Unclassified	18. SECURITY CLASSIFICATION OF THIS PAGE Unclassified	19. SECURITY CLASSIFICATION OF ABSTRACT Unclassified	20. LIMITATION OF ABSTRACT Unlimited	

## FOREWORD

Opinions, interpretations, conclusions and recommendations are those of the author and are not necessarily endorsed by the U.S. Army.

CAM Where copyrighted material is quoted, permission has been obtained to use such material.

CAM Where material from documents designated for limited distribution is quoted, permission has been obtained to use the material.

CAM Citations of commercial organizations and trade names in this report do not constitute an official Department of Army endorsement or approval of the products or services of these organizations.

\_\_\_\_ In conducting research using animals, the investigator(s) adhered to the "Guide for the Care and Use of Laboratory Animals," prepared by the Committee on Care and use of Laboratory Animals of the Institute of Laboratory Resources, national Research Council (NIH Publication No. 86-23, Revised 1985).

\_\_\_\_ For the protection of human subjects, the investigator(s) adhered to policies of applicable Federal Law 45 CFR 46.

\_\_\_\_ In conducting research utilizing recombinant DNA technology, the investigator(s) adhered to current guidelines promulgated by the National Institutes of Health.

\_\_\_\_ In the conduct of research utilizing recombinant DNA, the investigator(s) adhered to the NIH Guidelines for Research Involving Recombinant DNA Molecules.

\_\_\_\_ In the conduct of research involving hazardous organisms, the investigator(s) adhered to the CDC-NIH Guide for Biosafety in Microbiological and Biomedical Laboratories.

Carolyn A. MacDonald 9/29/98  
PI - Signature Date

## Table of Contents

Table of Contents .....	4
Introduction.....	5
Nature of the Problem.....	5
Purpose.....	5
Background.....	6
Benefits of Digital Mammography.....	6
Capillary Optics .....	6
Digital X-ray Detection.....	7
Proposed Statement of Work: Status.....	8
Progress to Date .....	9
Polycapillary Optics .....	9
Single Fibers .....	9
Transmission.....	9
Absorption Measurement .....	18
Collimating Optics .....	19
8 keV Prototype.....	19
Transmission and Uniformity .....	19
Divergence and Diffraction Gain .....	22
20 KeV prototype .....	23
Anti-Scatter Optics.....	25
Straight MultiFiber Optic.....	25
Magnifying Linear Monolithic Optics.....	26
Manufacturing Issues.....	30
Imaging Measurements .....	35
Artifact Reduction .....	36
Demagnifying, Focusing Monolithic Optics .....	39
Direct Digital Detectors.....	42
CZT Detector .....	42
Single pixel CZT detector .....	42
Linear array .....	44
CID Detector .....	46
Conclusions .....	47



## **Introduction**

### ***Nature of the Problem***

While it is hoped that molecular detection and intervention will one day provide a more effective treatment modality, currently, in the words of the Report to the U.S. Army Medical Research and Development Command on the Strategies for Managing the Breast Cancer Research Program, "no dominant etiology for breast cancer has emerged...[this] would lessen the prospects for any quick and easy prevention strategies.... mammography is the method of choice for screening women to detect breast cancer ... mammography has proven to be the most effective means of reducing breast cancer morbidity and mortality."

The primary theoretical limitations of mammography are the system resolution, which determines the minimum size of the detectable malignancy, and the need to expose the patient to ionizing radiation. Using innovative new technology to improve system resolution and reduce required dose will increase the effectiveness of this proven screening modality, with a direct and immediate impact on mortality. In addition, this direct digital system can avail itself of the advantages of digital processing, including improved image contrast and resolution at reduced radiation dose.<sup>1</sup> In practice, mammographic imaging is often limited by quality assurance issues, which can also be favorably addressed by digital processing.

### ***Purpose***

The overall objective of this proposal is to develop a mammographic system with extremely high scatter rejection and dynamic range, good resolution and low patient dose. This will be accomplished by developing a direct x-ray detector interfaced with a capillary x-ray optic in an appropriately designed mammographic system.

Kumakhov capillary x-ray optics, invented in the mid-eighties, provide an innovative new way to control x-ray beams. Such optics will provide extremely efficient scatter rejection, while allowing beam magnification, demagnification, and shaping to match with the newly developing high efficiency direct x-ray detectors. These detectors owe their high efficiency and resolution to the direct detection of x-ray photons without requiring phosphors for the conversion to visible light. An integrated system of optics and detectors will be developed in a highly collaborative effort involving recognized leaders in the fields of capillary optics, x-ray detectors, digital radiology, and mammography. Testing will be performed on each of the elements independently, and as an integrated unit in a mammographic system.

## Background

### Benefits of Digital Mammography

Conventional film/screen mammography suffers from limited dynamic range and film granularity, which can reduce the sensitivity of detection of microcalcifications. Digital detection provides high dynamic range, improving contrast, and greatly increasing the tolerance of the final image to under- or over-exposure. Digital images can be enhanced and are amenable to computer aided diagnosis. Spectral information can be included if it is available. Finally, digital images can be quickly transported for skilled consultation.

### Capillary Optics

Kumakhov capillary optics are bundles of hollow glass capillary tubes with inner diameters as small as a few microns. A typical fiber is shown in Figure 1. X rays incident on the interior of the glass tubes at small angles can be guided down the tubes by total external reflection.

The polycapillary fibers guide x rays in a manner analogous to the way fiber optics guide light. Arrays of curved tapered fibers can be used to focus, collimate and filter x-ray radiation.<sup>2,3,4,5,6</sup> Such arrays can be manufactured by stringing hollow glass polycapillaries through metal grids, as shown in Figure 24, or manufactured without grids as a monolithic optic, as shown in Figure 2.

The critical angle for total external reflection of x rays by glass polycapillaries is

$$\theta_c = \frac{\omega_p}{\omega}, \quad (1)$$

where  $\omega_p$  is the plasma frequency of the glass, about 30 eV, and  $\omega$  is the photon frequency. The critical angle is 1.5 milliradians at 20 keV. The x rays can be transmitted in a curved tube so long as the tube is small enough and bent gently enough that the angles of incidence are kept less than the critical angle. For a given radius of curvature, this requires increasingly small diameter tubes as the x-ray energy is raised. In order to avoid the mechanical limitations of such small tube sizes, polycapillary fibers are employed with channel sizes (typically 1-30  $\mu\text{m}$ ) much smaller than the outer diameter (300-1000  $\mu\text{m}$ ).

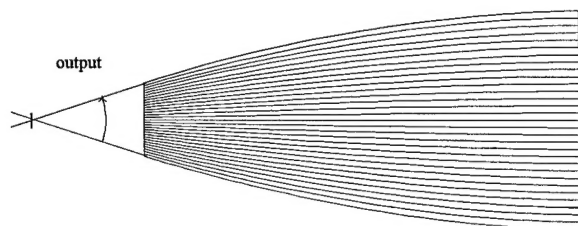


Figure 2. Monolithic optic geometry.

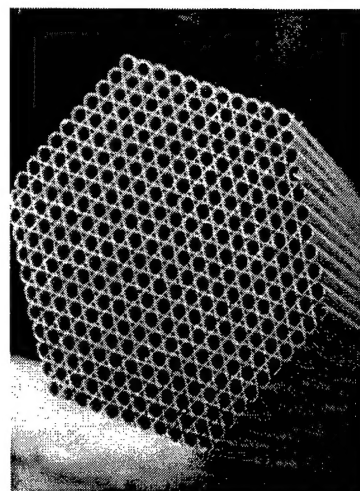


Figure 1. Cross sectional scanning electron micrograph of polycapillary fiber 0.5 mm in diameter.

The use of Kumakhov capillary optics in place of more conventional scatter reduction grids in a mammographic system has significant potential to provide improved resolution, increased contrast enhancement, and reduced dose in mammographic imaging. The optics can also be used to mate the radiographic image with a digital detector by appropriate

choice of magnification, demagnification, or separation to discrete chips. In addition, a pre-patient optic could be employed to increase the available intensity in a fan beam relative to simple slot collimation.

### Digital X-ray Detection

In almost all radiological systems, detection of x rays is performed by the use of a "phosphor" screen which converts absorbed x rays into visible light photons. The visible light is then recorded on an analog medium, such as film, or detected by a digital detector. The phosphor screen is used because most detectors, including film, are not particularly sensitive to x rays. The use of a screen-film combination reduces radiation requirement compared to direct exposure film by a factor of 50-100.<sup>7</sup> This increase in sensitivity occurs at the expense of resolution. The modulation transfer function of a good film-screen combination drops to less than 0.1 at a frequency of 15 lp/mm.<sup>7</sup> The choice of screen thickness is a trade-off between detected quantum efficiency, which improves with increasing thickness, and resolution, which is degraded by light blur in a thick screen.<sup>8</sup>

Efficient direct x-ray detection virtually eliminates the tradeoff between spatial resolution and sensitivity because of the elimination of the phosphor screen. Direct x-ray detectors can provide resolution of 20 lp/mm or better with nearly 100% Detector Quantum Efficiency (DQE).

An especially promising direct x-ray detector is the cadmium zinc telluride (CZT) semiconductor detector recently developed by Digirad, formerly Aurora Technologies. The DQE of a .5 mm thick CZT detector is essentially unity at 20 keV, while the resolution is to first order independent of thickness. CZT detectors are similar in many respects to cadmium telluride (CdTe) detectors which have been available commercially for many years. The replacement of a fraction of the Cd with Zn causes a wider bandgap and results in a resistivity increase of two orders of magnitude. This high resistivity is an important factor because it reduces leakage current, a significant source of performance degrading noise. Leakage current noise generally limits the use of CdTe detectors by requiring longer integration times and larger pixel sizes.

Another promising direct digital detector is the Charge Injection Device (CID). Like the more common CCD (Charge couple device) CID technology allows for rapid array imaging. Unlike the CCD, the CID is very radiation resistant. Also unlike CCDs, for which the entire array must be read out and simultaneously cleared as a unit, CID pixels can be read individually, repeatedly, and nondestructively, leading to very high dynamic range. CID pixel well depths are also deeper than conventional CCDs, leading to a substantial reduction in blurring from high energy x-ray photons.

***Proposed Statement of Work: Status***

- I. Development of Capillary Optic Mammographic System: Months 1-36
  - I.A. Single Capillary Measurements: Months 1-6: Completed
  - I.B. Simulation of Design Strategies: Months 6-18: Completed
  - I.C. Assembly and Testing of Prototype Optic: Months 18-24: Completed
  - I.D. Design of Final Mammographic Optics and Detector Unit: Months 20-28: 90% Completed
  - I.E. Assembly and Testing of Final Optic: Months 28-36: Delayed, Ongoing
- II. Development of Digital Detector: Months 1-24
  - II.A. Fabricate CZT Linear Detector Arrays: Months 1-24: Completed
  - II.B. Develop Interconnect Methodology (Wire Bonding): Months 2-8: Completed
  - II.C. Assemble and Test Proof of Principle Detector/Multiplexer Hybrid : Months 2-12: Completed
  - II.D. Assemble Additional Hybrid Arrays: Months 12-24: Changed
- III. Mammographic Measurements: Months 18-48
  - III.A. Measurement of Prototype System: Months 18-36: Completed
    - III.A.1 Design and Fabrication of Test System: Months 18-24: Completed
    - III.A.2. Measure Primary Transmission in a Mammographic Geometry: Months 24-30: Completed
    - III.A.3 Measure Transmission of Scattered Radiation: Months 24-30: Completed
    - III.A.4. Spectral Measurements: Months 24-30: Completed
    - III.A.5. Investigate Artifacts due to Capillary Structure: Months 30-36: Ongoing
    - III.A. 6. Measure Contrast Improvement and Resolution: Months 30-36: Completed
  - III.B. Measurement of Final Optics/Detector System: Months 28-48
    - III.B.1. Design and Fabrication of Measurement System: Months 28-36: Completed
    - III.B.2. Measure Primary Transmission in a Mammographic Geometry: Months 36-42: Ongoing
    - III.B.3. Measure Transmission of Scattered Radiation: Months 36-42: Ongoing
    - III.B.4. Spectral Measurements: Months 36-42: Ongoing
    - III.B.5. Investigate Artifacts due to Capillary Structure: Months 42-48: Ongoing
    - III.B.6. Measure Contrast Improvement and Resolution: Months 42-48: Ongoing
    - III.B.7. Evaluate Image Quality Using RMI Breast Phantom: Months 42-48: Future

### Progress to Date

Rather than follow a step by step task listing, this progress report has been divided into subject areas to provide a more coherent description of the current state of the art. While there has been substantial manufacturing delays in the production of monolithic optics, the available optics have lent themselves to a thorough systematic review of the various optics geometries proposed for this project. Representative measurements have been made on a large number of optics geometries, rather than relying on the simple simulations initially proposed for this project. Manufacturing issues are discussed as well. A decision has been made to concentrate on two geometries, a collimating optic with a prepatient monochromatizing crystal, and a "multi-taper" post patient optic assembled of three smaller tapers to produce a larger area optic without the technological problems of a single large area glass bundle. Manufacturing delays have led to a granted no cost extension of this project.

The proof-of-principle linear CZT array has been demonstrated, but an alternate detector path, CID technology appears equally promising. Studies of both detectors are discussed.

### Polycapillary Optics

Measurements and simulations have been performed on several geometries: single fibers; multifiber collimating optics; multifiber straight antiscatter optics; and magnifying and demagnifying monolithic optics.

#### Single Fibers

##### TRANSMISSION

An important step in optics development was the breakthrough in modeling capacity, which has led to an unprecedented level of theoretical understanding of the basic properties of polycapillary fibers, especially fiber defects. To evaluate the experimental performance of polycapillary fibers, and design capillary optics, it is necessary to be able to predict theoretical behavior for complex geometries. The modeling program for single fibers is based on a Monte Carlo simulation of simple geometrical optics. The computational speed is greatly enhanced by a reduction to two dimensions by projecting the trajectory onto the local fiber cross-section.<sup>9</sup> Reflectivities are computed from standard tables.<sup>10</sup> Significant recent progress has been made in understanding the effect of capillary profile error, waviness, and roughness on the transmission spectra.<sup>11</sup> This is extremely important in providing feedback to the

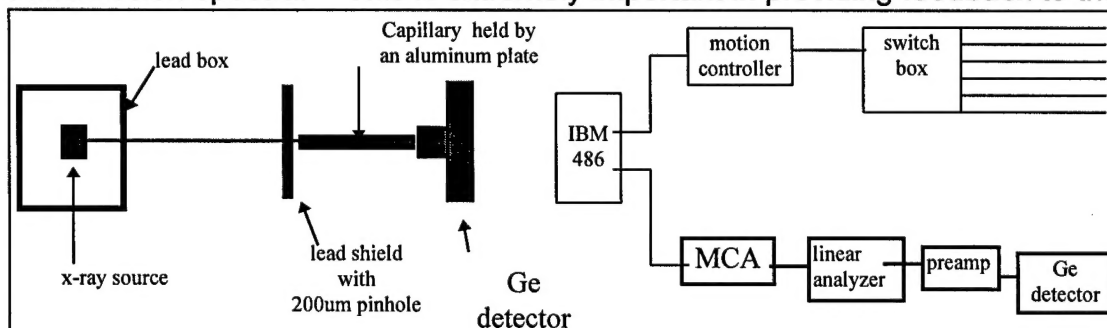


Figure 3. Experimental setup.

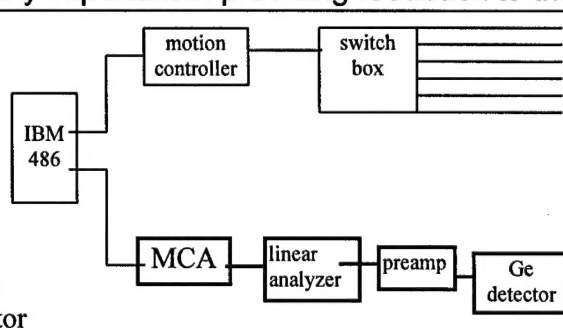


Figure 4. Electronic system.

Type	Description	Outer Diameter, mm	Channel Size, $\mu\text{m}$	Open Area	Length, mm
A	Borosilicate	0.5	12	65%	105
B	Lead glass	0.5	12	52%	95
C	Borosilicate	0.75	22	50%	136
D	Borosilicate	4	12	55%	130
E	Borosilicate	0.3	4-5	55%	105

Table 1. Description of polycapillary fibers.

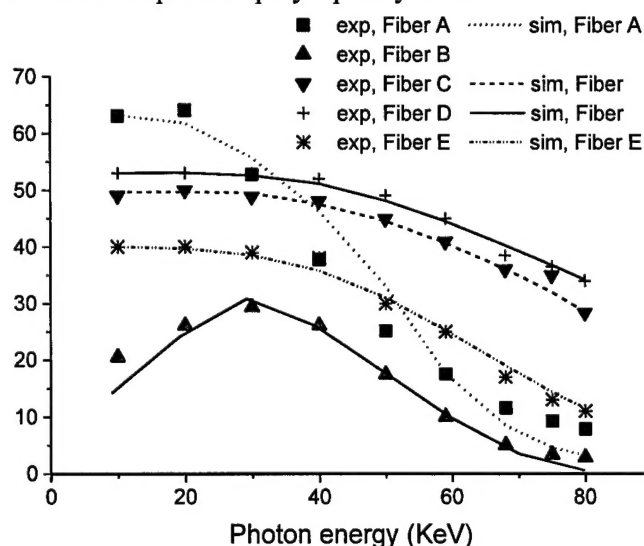


Figure 5. Measured transmission versus energy for polycapillary fibers listed in Table 1.

dimensions. A collimator is placed before the fiber and any remaining x-ray leakage around the fiber is eliminated with metal powder or filings. The measured fibers are described in Table 1.

The results of transmission studies as a function of photon energy are shown in Figure 5.<sup>13,14</sup> All of the fibers except the lead glass have transmissions at 20 keV nearly equal to their fractional open area (the fraction of the cross section of the capillary which is open space, the rest being glass walls). This transmission corresponds to the primary transmission expected for a linear capillary optic employed as an antiscatter grid.

manufacturing process. In the last year, it has been found that extremely good fits can be produced with only two fitting parameters if a more physical model of waviness is employed.<sup>12</sup>

The experimental arrangement for single capillary measurements is shown in Figure 3 and Figure 4. An optical rail affixed to an optical table carries an x-ray source, fiber platform, and x-ray detector. Each can be positioned independently in three

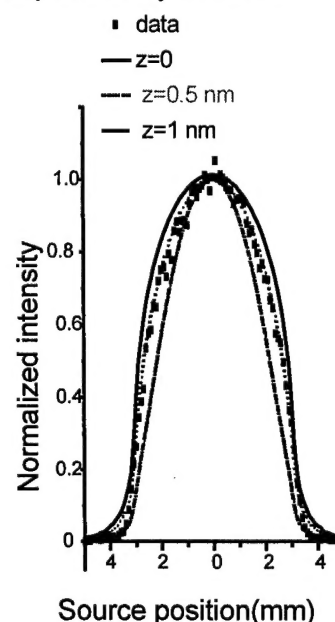


Figure 6. Source scans at 10 keV.



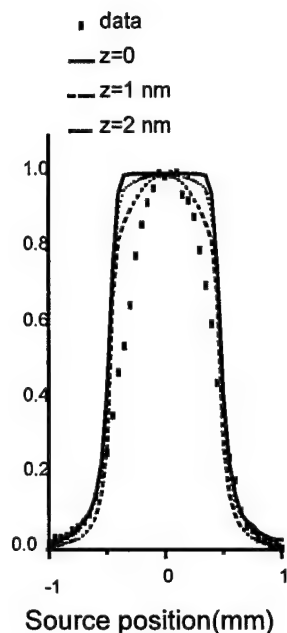


Figure 7. Source scans at 68 keV.

The transmission falls off at higher energies. Modeling this transmission spectra has lead to a greater understanding of defects in polycapillary optics.

In Figure 6, simulations with or without roughness corrections are compared with the experimental data. In these measurements the source is scanned transverse to the fiber axis. The simulation with a roughness height of 0.5 nm fits the experimental data quite well. It is definitely over-corrected when the roughness is 1.0 nm. The same simulations, shown in Figure 7, are also carried out at 68 keV, where the width of the curve is narrower than that at 10 keV because of the smaller critical angle. As a result, photons also experience fewer bounces on average. Simulations with roughnesses as large as 1.0 and 2.0 nm still could not fit the data. Knowing that 1.0 or 2.0 nm roughness is definitely too large at 10 keV, we can determine that the roughness correction by itself is not sufficient at high energy to reproduce source scan measurements. Other effects need to be considered. These are bending and waviness.

A slight bending of the capillary can dramatically reduce the transmission of high energy photons because of the small critical angle. A comparison between experimental data and simulations with different bending is shown in Figure 8. The figure shows that the simulations with bending alone do not fit the experimental data well, which indicates that bending is not the only factor which causes the high energy

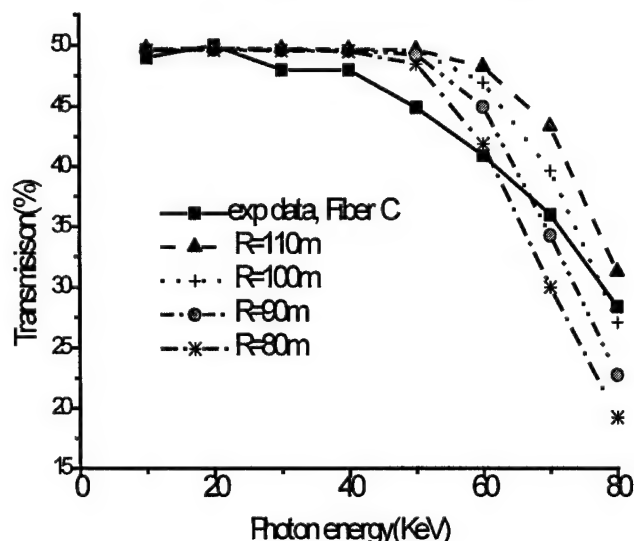


Figure 8. Transmission spectra of Fiber 3 simulated with different bending curvature alone and compared with experimental data

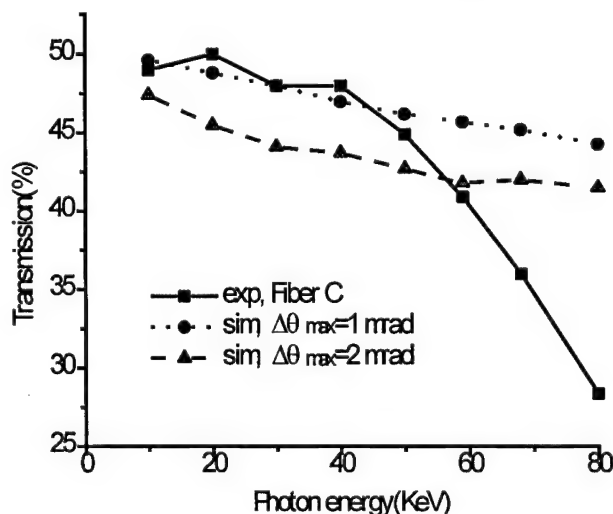


Figure 9. Simulations of transmission spectra with waviness only compared with the experimental data.

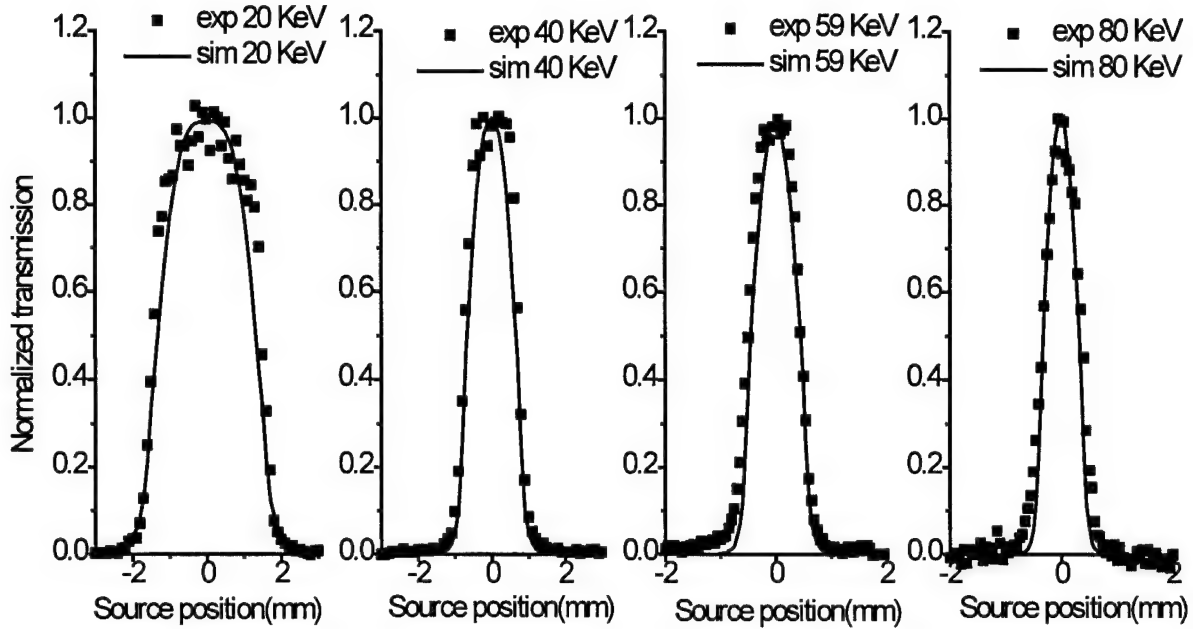


Figure 10. Simulated source scan curves compared with experimental data at four different photon energies. Parameters are:  $R = 125$  m,  $\Delta\theta_{\max} = 0.35$  mrad, roughness height = 0.5 nm.

transmission to drop. However, from Figure 8, we can see that the range of the bending radius must be larger than 100m to give the observed transmission at the highest energy(80KeV).

Capillary surface oscillations with wavelengths shorter than the capillary length and longer than the wavelength of the roughness are called waviness. The detailed shape of waviness is unknown. Its average effect can be considered as a random tilt of the glass wall, so that the grazing angle of the photon is changed by a random amount,  $\delta\theta$ , after every bounce.  $\delta\theta$  is a random number between  $-\Delta\theta_{\max}$  and  $\Delta\theta_{\max}$  if  $\theta \geq \Delta\theta_{\max}$ . The maximum random tilt angle  $\Delta\theta_{\max}$  is an adjustable parameter which depends on the waviness of the polycapillary fiber. To keep  $\theta'$

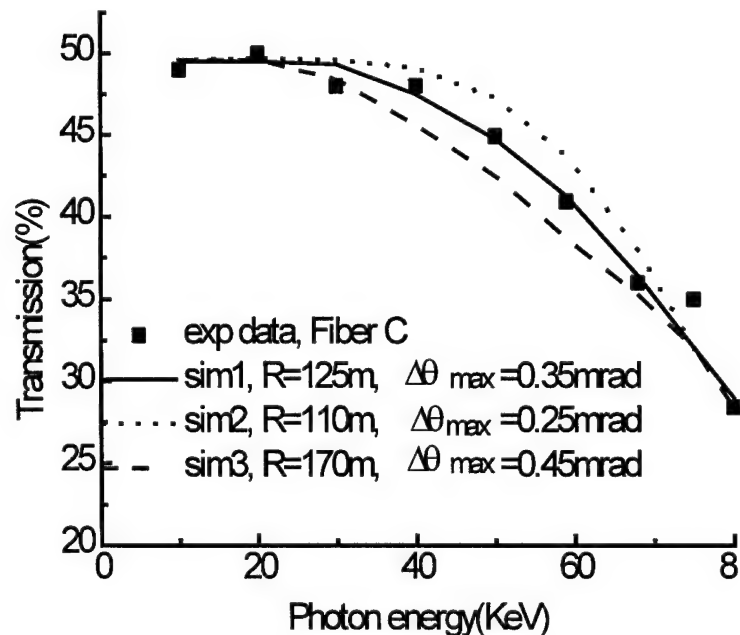


Figure 11. Simulated transmission spectra with different bending and waviness compared with the experimental data in search for the best fitting of Fiber C.



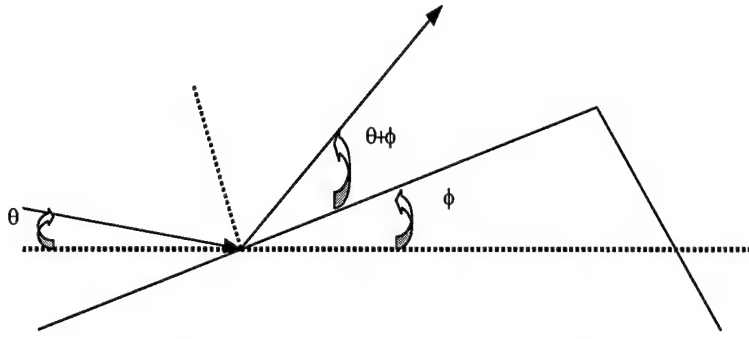


Figure 12. Scheme of an x-ray beam interacts with a random tilt surface.

positive,  $\delta\theta$  is taken to be a random number between  $-\theta$  and  $\Delta\theta_{\max}$  when  $\theta < \Delta\theta_{\max}$ . Since a photon with an incident angle smaller than  $\Delta\theta_{\max}$  has a larger chance to experience an angle increase than an angle decrease, this is physically reasonable. In Figure 9, simulations with waviness corrections with  $\Delta\theta_{\max}$  set at 1 mrad and 2 mrad, which is comparable to the critical angle, are compared with the

experimental data. This figure shows that simulations with waviness alone do not fit the experimental data. This is because the waviness correction changes the reflected angle, not the profile. In fact the capillary is still considered to be straight, so those photons which have few reflections will not be significantly effected by waviness.

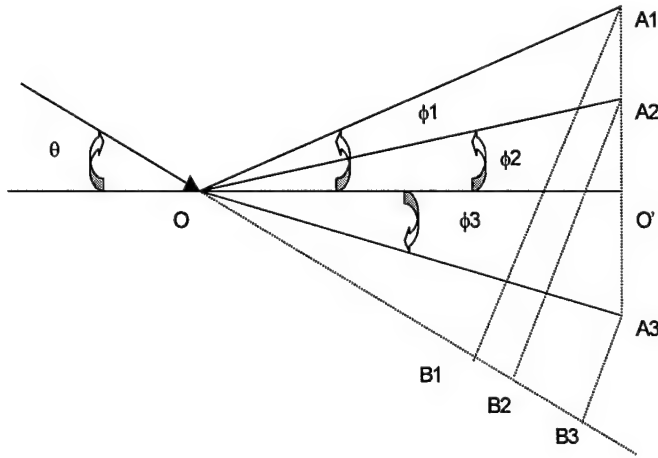


Figure 13. Three surfaces, OA1, OA2 and OA3, with different tilt angles,  $\phi_1$ ,  $\phi_2$  and  $\phi_3$ , respectively, from the nominal surface  $OO'$ .

Finally the waviness and bending are combined by increasing the bending radius  $R$ , roughly determined in Figure 8, and adding a waviness parameter,  $\Delta\theta_{\max}$ . Several trials are shown in Figure 11. Sim2 has too much bending and not enough waviness; sim3 has too much waviness and not enough bending; sim1 is the best fit. Roughness is also included in those simulations. The source scan

simulation with the three fixed parameters are plotted along with the experimental data in Figure 10 for four more photon energies. They all fit quite well. This model, hereafter labeled M1, assumed a uniform distribution of tilt angles, which is not quite physical. In more recent work, discussed as Model M2, it is assumed that these tilt angles,  $\phi$ , are normally distributed in the range  $(-\pi/2, \pi/2)$  with the mean value equal to zero. For high quality optics, the standard deviation of this normal distribution,  $\sigma$ , is much smaller than the critical angle,  $\theta_c$ . The probability distribution of tilt angles,  $\phi$ , is

$$G(\phi) = \frac{1}{\sigma\sqrt{2\pi}} e^{-\frac{\phi^2}{2\sigma^2}}. \quad (1)$$

In this work, Model M2, consideration was taken of the fact that the surface tilt angle will affect the probability of x-ray impact on that surface. Taken to extremes, a surface region perpendicular to the beam is much more likely to intercept the beam than a surface region parallel to the beam. Figure 13 displays three surfaces,  $OA_1$ ,  $OA_2$  and  $OA_3$ , with different tilt angles,  $\phi_1$ ,  $\phi_2$  and  $\phi_3$ , respectively, from the nominal surface  $OO'$ . The projections onto the nominal surface for the three surfaces are equal,  $OA_1 \cdot \cos\phi_1 = OA_2 \cdot \cos\phi_2 = OA_3 \cdot \cos\phi_3 = OO'$ . The probability of incidence of a parallel x-ray beam with incident angle  $\theta$  (with respect to the nominal surface  $OO'$ ) hitting these tilted surfaces is given by their corresponding perpendicular length  $A_j B_j$  (for  $j = 1, 2$  or  $3$ )

$$P_j \propto A_j B_j = OA_j \cdot \sin(\theta + \phi_j) = \frac{OO'}{\cos\phi_j} \cdot \sin(\theta + \phi_j), \quad (2)$$

We call this the tilt-corrected probability distribution. The complete description of this distribution is

$$H(\phi) = \begin{cases} \frac{F \sin(\theta + \phi)}{\cos(\phi)}, & -\theta < \phi < \frac{\pi}{2} \\ 0, & -\frac{\pi}{2} < \phi \leq -\theta \end{cases}, \quad (3)$$

where  $\theta$  is the incident angle,  $\phi$  is the tilt angle and  $F$  is a normalization constant.

Combining the normal distribution  $G(\phi)$  with the tilt correction  $H(\phi)$  gives  $\phi$  for a certain incident angle  $\theta$  as follows:

$$J(\phi) = \begin{cases} K e^{\frac{-\phi^2}{2\sigma^2}} \cdot \frac{\sin(\theta + \phi)}{\cos\phi}, & -\theta < \phi < \frac{\pi}{2} \\ 0, & -\frac{\pi}{2} \leq \phi \leq -\theta \end{cases}, \quad (4)$$

where  $\theta$  is the incident angle,  $\phi$  is the tilt angle and  $K$  is a normalization constant.

Noting that

$$\frac{\sin(\theta + \phi)}{\cos\phi} = \sin\theta + \cos\theta \cdot \tan\phi \quad (5)$$

and that both the incident angle,  $\theta$ , and the tilt angle,  $\phi$ , are very much less than 40 mrad, we use the approximation

$$P(\phi) = \begin{cases} C e^{\frac{-\phi^2}{2\sigma^2}} * (\theta + \phi), & -\theta < \phi < \frac{\pi}{2} \\ 0, & -\frac{\pi}{2} \leq \phi \leq -\theta \end{cases}, \quad (6)$$

where the normalization constant,  $C$ , is

$$C \approx \frac{1}{\sqrt{2\pi\theta\sigma + 2\sigma^2}}, \quad (7)$$

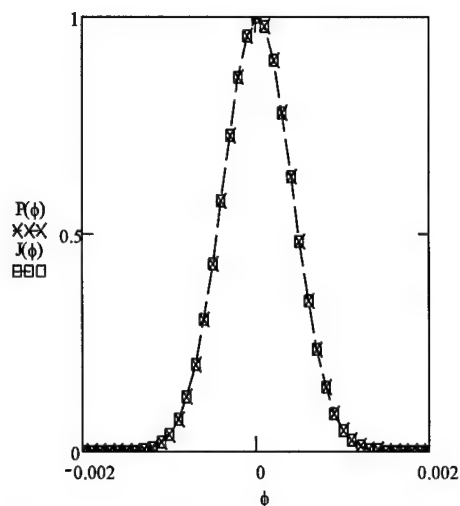


Figure 14.  $P(\phi)$  and  $J(\phi)$  versus tilt angle  $\phi$  when incident angle  $\theta = 0.009\text{rad}$ , standard deviation  $\sigma = 0.0004\text{rad}$ .  $\phi$  is in rad.

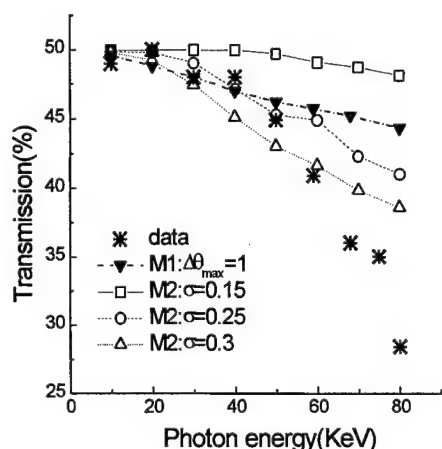


Figure 15. Simulations of transmission spectra for fiber C with only waviness compared with the experimental data. This figure shows the effects of waviness. It also shows simulations using waviness alone do not fit the data. The simulations do not include roughness or bending.

to speed the calculation.  $P(\phi)$  is called the tilt-corrected normal distribution. In model M2,  $\sigma$  is the variable that describes the amount of waviness. An example of  $J(\phi)$  and  $P(\phi)$  is shown in Figure 14. The result of the waviness calculation is shown in

Figure 15. The model M2 shows a much larger drop at high photon energies for lower values of the waviness than does model M1. A comparison of the simulation with bending and waviness to the experimental data is shown in Figure 16.

Using a similar technique, the simulation was compared to the fibers listed in Table 1, using the parameters listed in Table 2. The results are plotted in Figure 17 and Figure 18. In Figure 17, the transmission for fiber A shows a rapid drop for energies above 30 keV. Although fiber D has lower fractional open area than fiber A, its transmission exceeds that of fiber A at energies above 30 keV. This is because fiber A

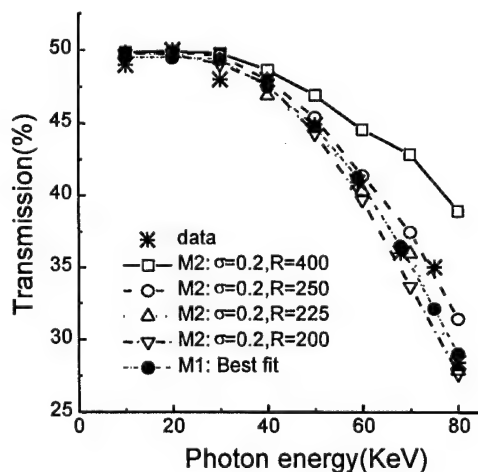


Figure 16. Simulated transmission spectra using model M2 with fixed waviness ( $\sigma=0.2\text{ mrad}$ ) and different bending (bisection method), compared with the experimental data. The simulation curves shown are just a few representative cases in the bisection process. For M2, the best-fit parameters are  $\sigma = 0.2\text{ mrad}$  and  $R = 225\text{ m}$ ; for M1, they are  $z = 0.5\text{ nm}$ ,  $s = 6\text{ }\mu\text{m}$ ,  $\Delta\theta_{\text{max}} = 0.35\text{ mrad}$  and  $R = 125\text{ m}$ .

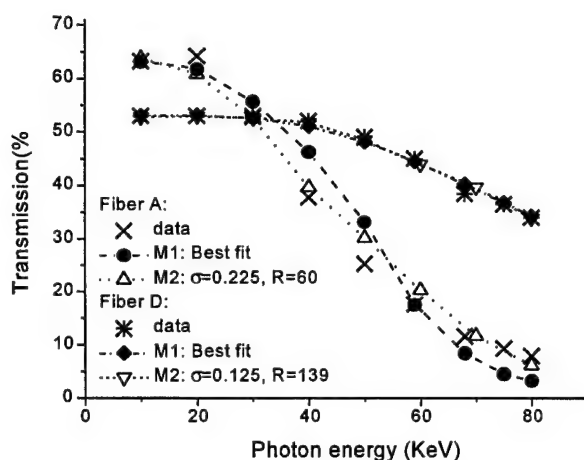


Figure 17. Simulations of transmission spectra of fiber A and fiber D with their best-fit parameters compared with the experimental data. All parameters related to this figure are listed in Table 1.

transmission about the same as for fiber C.

Fiber E is the thinnest fiber. Table 2 shows that it has the largest bending correction because of its flexibility. Its transmission curve is flat up to 40 keV. This is due to its very small channel size, as discussed in the comparison of fiber C and fiber

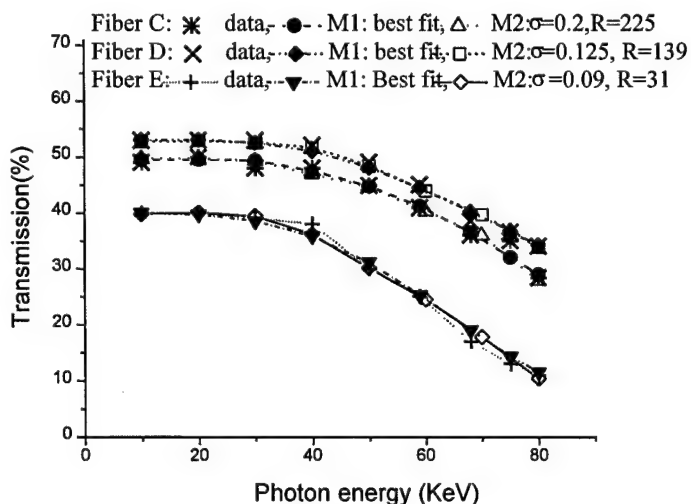


Figure 18. Simulations of transmission spectra of fiber C, fiber D and fiber E with their best-fit parameters compared with the experimental data. All parameters related to this figure are listed in Table 2.

is thin (0.5 mm in outer diameter) and flexible, therefore difficult to keep straight in the measurement apparatus. Model M2, which can vary only bending and waviness, requires a much sharper bend for fiber A than for fiber D. This bending is more significant at high energies, where the critical angles are smaller.

Transmission curves for fiber C and D are similar in shape and are nearly flat up to 60 keV, as shown in Figure 18. However, the smaller channel size for fiber D results in the simulation being less sensitive to bending. Therefore a larger bending curvature (smaller radius) is required for fiber D. The waviness correction for fiber D must therefore be smaller to keep the

transmission about the same as for fiber C. However, if the channel size is too small, as in fiber E, it also results in more reflections being needed for a photon to traverse the fiber and may have introduced other defects such as blocked channels. This is why the transmission is only 40% for the energies below 40 keV although the open area is around 55%.

The new model yields as high a quality fit with two fewer fitting parameters than used in model M1 in Figure 5. The high transmission and the simulation results show that the quality of the capillary fibers is quite good. The bending radius is above 130 meters for type 3 and type 4 capillaries. It is hopeful that we

Fiber Description						Model M1				Model M2	
Fiber #	Type	Outer Diameter (mm)	Channel Size ( $\mu\text{m}$ )	Area	Length (mm)	z nm	s $\mu\text{m}$	R m	$\Delta\theta_{\text{max}}$ mrad	R m	$\sigma$ Mrad
A	1	0.5	12	65%	105	0.7	6	105	0.4	60	0.225
C	3	0.75	22	50%	136	0.5	6	125	0.35	225	0.2
D	4	4	12	55%	130	0.8	6	110	0.285	139	0.125
E	5	0.3	4-5	55%	105	0.7	6	28	0.2	31	0.09
F	4	4	12	55%	130	0.8	6	90	0.45	90	0.18

Table 2 Parameters for best-fit simulations.  $R$  is the bending radius. For M1,  $\Delta\theta_{\text{max}}$  is the amount of waviness,  $z$  is the roughness height and  $s$  is the roughness correlation length. For M2,  $\sigma$  is the standard deviation of the waviness.

can further improve the high-energy transmission performance of polycapillary fibers by decreasing to an optimum channel size, and making them more rigid.

Fiber B in Figure 5 has poor transmission; it is a lead glass fiber, with high surface roughness and waviness. More recently, higher quality lead glass fibers have been produced. The transmission as a function of photon energy for these fibers is shown in Figure 19. These leaded fibers have higher absorption of high angle photons than the lower density borosilicate glass fibers, and therefore would provide even better scatter rejection.

Transmission was also measured of deliberately curved fibers, which can be used to deflect x-ray beams over larger angles. The results are shown in Figure 20. Simulated

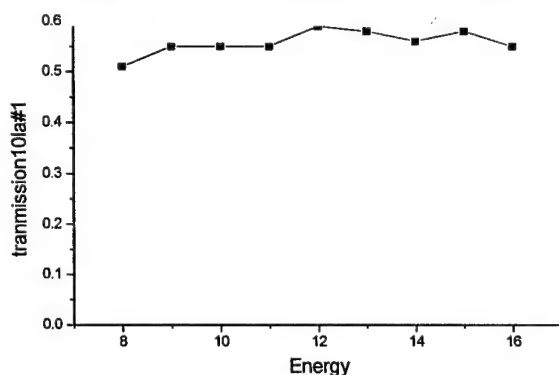


Figure 19. Recently manufactured lead glass fibers.

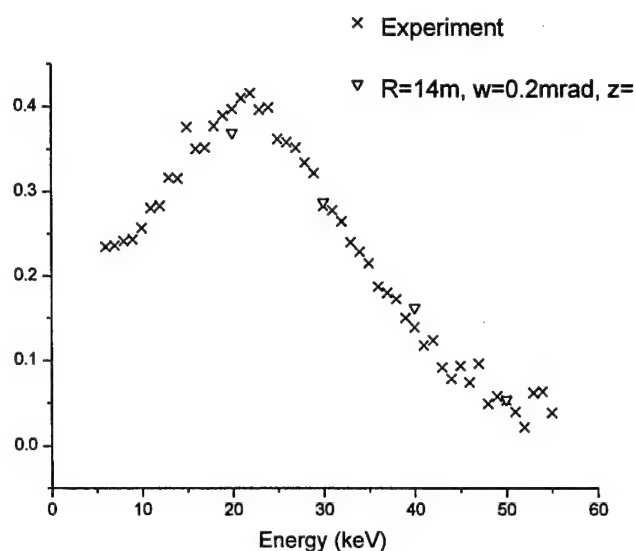


Figure 20. Transmission efficiency of 350  $\mu\text{m}$  OD polycapillary fiber with 6  $\mu\text{m}$  channel diameter. The fiber length is 25 cm. Simulated values are shown for 20, 30, 40, 50 keV x rays. The parameters are curvature,  $R$ ; waviness,  $w$ ; and roughness,  $z$ .

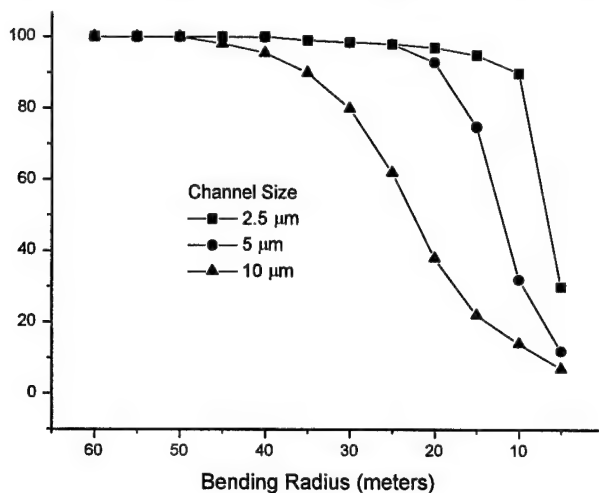


Figure 21. Simulated transmission as a function of bending radius at 50 keV, with no waviness or roughness.

the critical angle.

The setup includes a source, a pinhole with size of 200  $\mu\text{m}$ , an aluminum plate which is used to hold the capillary bundle, and a Germanium detector. The source has a maximum operate voltage of 100 kV. The source and aluminum plate are attached on linear stages which are controlled by linear actuators. Both the source and the optics fiber can move freely in two perpendicular directions transverse to the x-ray beam. An additional rotary stage is used to rotate the aluminum plate, so that the optic can also be rotated in horizontal direction.

The experiment starts with the alignment between the source, pinhole, and detector, by adjusting the source and fiber positions. After alignment, the optic was tilted to an angle larger than the largest critical angle for the measured energy range, then translated out of the x-ray beam. While the capillary optics was moved into the x-ray beam step by step, an x-ray spectrum was taken by the germanium detector after the optics at each step. The acquire time for each step was 30 seconds. The transmission at every step is the ratio

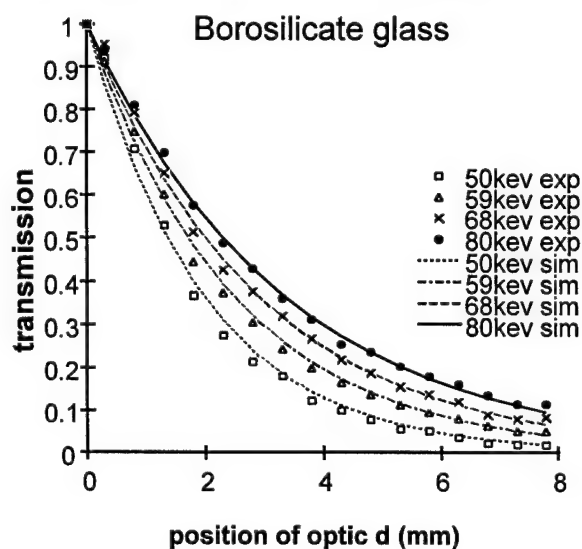


Figure 22. Absorption measurement

transmission for a single fiber with various channel sizes is shown in Figure 21.

### ABSORPTION MEASUREMENT

To achieve total scatter rejection, the glass wall of the optics must be thick enough to absorb the scattered x rays from various directions while allowing the majority of the primary x rays to pass. The absorption of the polycapillary fiber bundle was measured by tilting the optic to an angle which is larger than

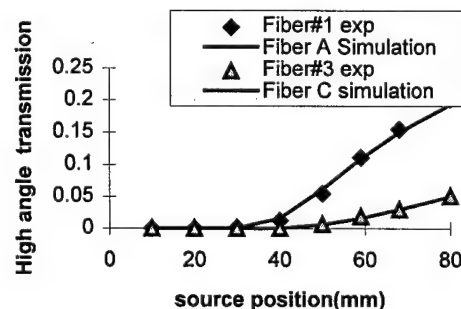


Figure 23. High angle transmission through capillary walls as a function of photon energy.

between the counts without optics and the counts with optics at that step. Transmission at different energies as a function of optic position is plotted in Figure 22 along with the theoretically calculated values.

Large angle transmission can be calculated as

$$T_s = e^{-(1-f) \cdot \mu \cdot \rho \cdot x} \quad (2)$$

where  $\mu$  is the mass attenuation of the material which can be calculated from tabulated values<sup>21</sup> according to the mass composition,  $\rho$  is the density of the glass,  $f$  is the open area of the capillary bundle, and  $x$  is the distance that the x-ray beam travels across the fiber.  $x$  can be calculated from capillary movement  $d$  and capillary tilting angle,

$$x = d / \alpha, \quad (3)$$

where  $\alpha$  is the tilting angle in rad.

Theoretical calculated numbers from equation (2-3) are compared with the experimental result in Figure 22. The theoretical values fit well with the experimental data. Measured and theoretical transmission of a polycapillary fiber as a function of photon energy is shown in Figure 23. This "high angle transmission" corresponds to scatter transmission for the capillary optics used as an antiscatter grid, and is less than 1% at 20 keV. The solid lines are theoretical calculations, which agree quite well with the data. Lead glass optics would have even better scatter rejection, as shown in Figure 25.<sup>15</sup>

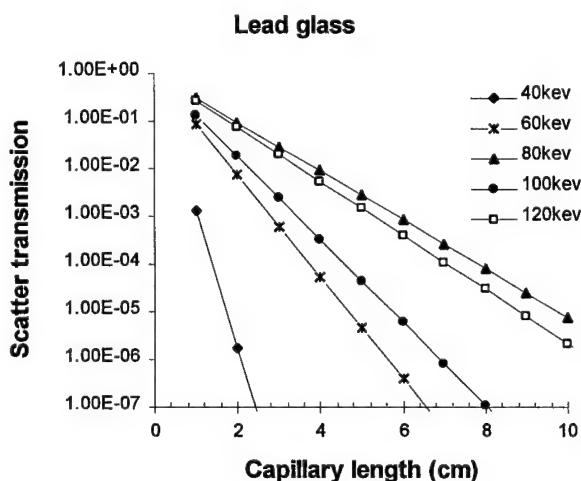


Figure 25. Calculated scatter transmission for lead glass optics of various lengths.

## Collimating Optics

### 8 KEV PROTOTYPE

#### Transmission and Uniformity

Because of the technological difficulties in producing large area monolithic optics, the fastest route to a large scale antiscatter system for contrast measurements is a straight optic.

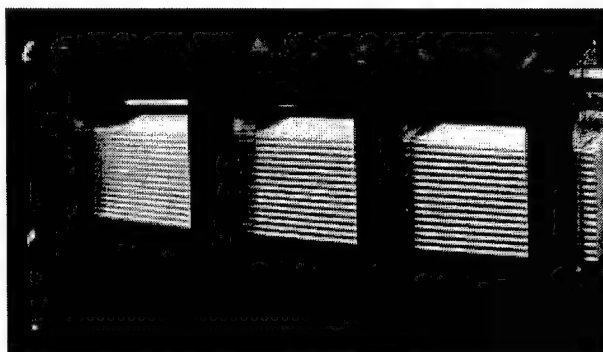


Figure 24. Multifiber collimating lens.

The low angular acceptance of the capillary channels requires that such an optic be used with a collimated beam, as shown in Figure 26. A collimating lens, similar to that pictured in Figure 24, and a straight fiber bundle of 3 cm diameter have been obtained. The collimating lens has an output diameter of 3 cm, a focal distance of 150 mm, and collects from an angle of  $8^\circ$ . It was designed for 8 keV, where the transmission is 30%, but has a transmission of 14% at 20 keV. The drop off is due to the reduction in critical angle for reflection with x-ray energy, as stated in equation (1). Because this optic would be used prepatient, low transmission would not increase dose, only increase tube loading. More importantly, as will be demonstrated in the next section, a lens actually designed for 20 keV would have a higher transmission at that energy. The primary purpose of studying this lens is to develop experience with large

scale polycapillary optics and refine the modeling to increase the confidence in the simulations. The simulated and measured transmission of the lens as a function of source to lens distance is shown in Figure 27. The simulation, which models the complex geometries of complete lenses, was developed by X-ray Optical Systems, Inc. Some delay in the commencement of the simulation task was created by the necessity of assuring the confidentiality of the proprietary code while providing access to student researchers. Access has been provided, and comparisons of measurements and simulations of a collimating lens have given good results. The

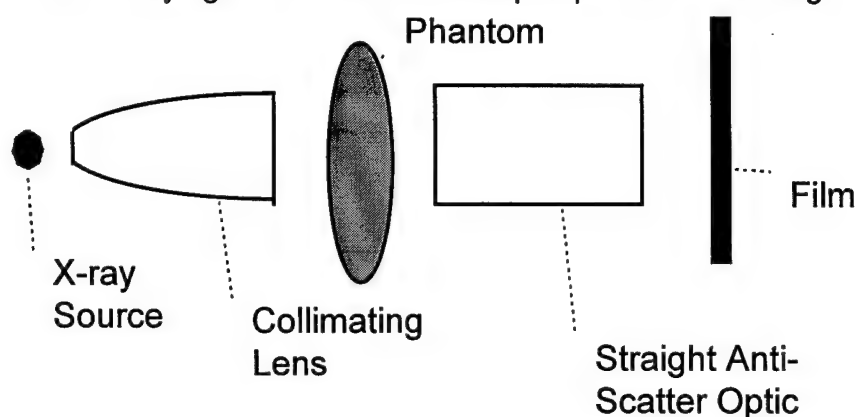


Figure 26. Set-up for Anti-scatter measurements.

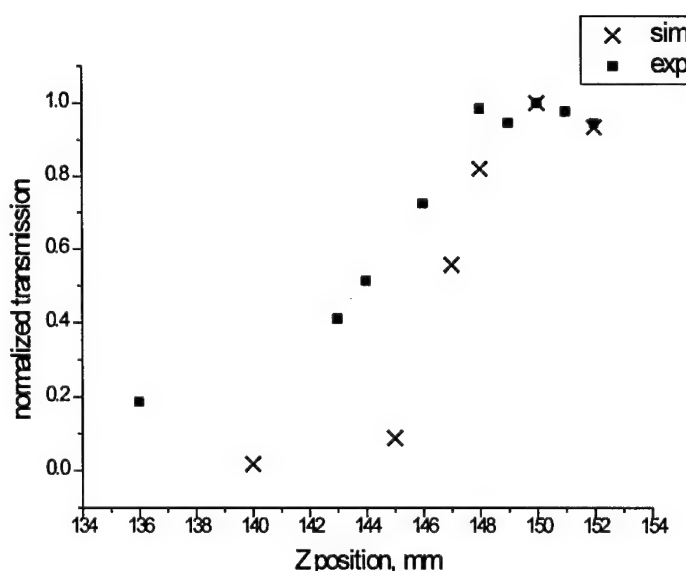


Figure 27. Variation in measured (box) and simulated (x) 20 keV transmission as the source is moved towards the lens along the fiber axis.



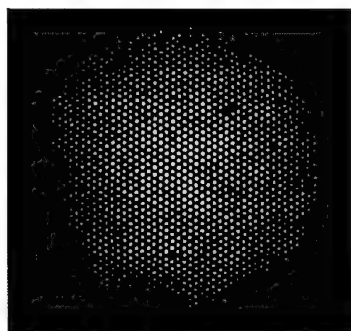


Figure 28. X-ray photograph of output of collimating optic.

measured and simulated transmission as a function of photon energy for the lens (with the central part blocked, as shown in Figure 29), is shown in

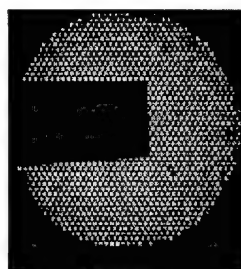


Figure 29. X-ray photograph of output of 8 keV collimator. A rectangular lead sheet blocks part of the output.

Figure 31.

More serious for imaging experiments than the low transmission of a lens designed for lower energies, is the non-uniformity of the field. The outer fibers are bent too much to permit good transmission at these energies. The fall off in transmission can be seen in the photograph shown in Figure 28, and in the simulation of Figure 30. Contrast enhancement

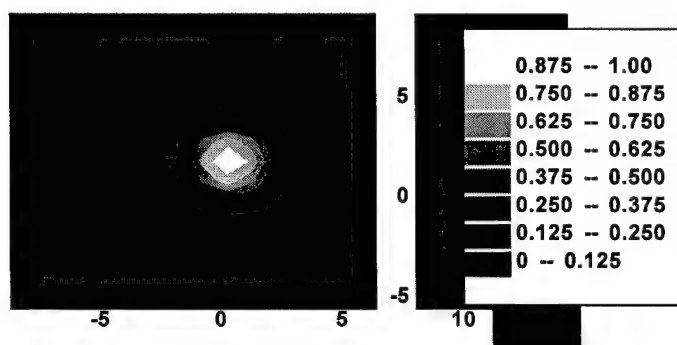


Figure 30. Simulated output, at 20 keV, of collimator designed for 8 keV.

measurements, which are ongoing, must take these nonuniformities into account. Figure 29 shows the output of the lens after a center section was blocked. This section contains fibers which were removed for study of radiation exposure effects after extensive exposure to intense synchrotron radiation.<sup>16,17</sup> The radiation effects were found to be manageable and are not expected to be significant for

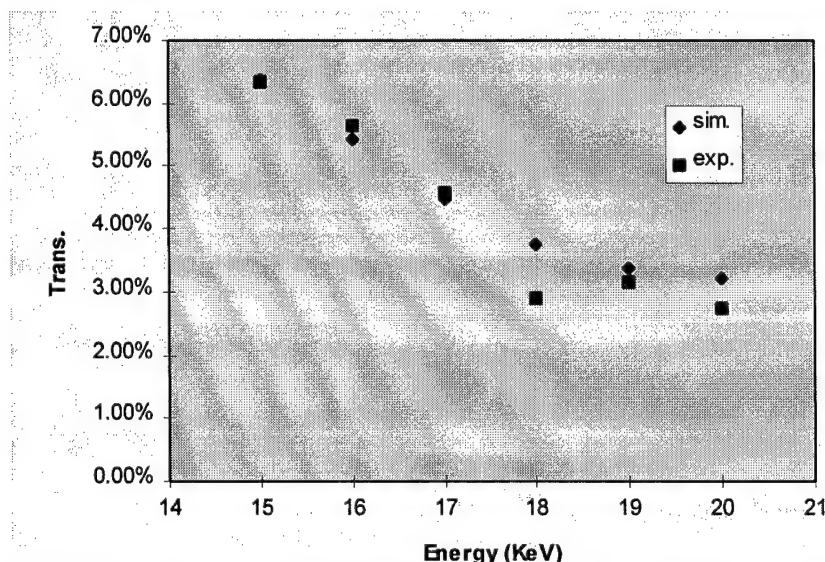


Figure 31. Transmission of 8 keV collimator as a function of photon energy. The simulation assumes a fiber open area of 65%, the fibers packed to fill 50% of the lens input area, and  $\frac{1}{4}$  of the lens blocked by the lead shield..

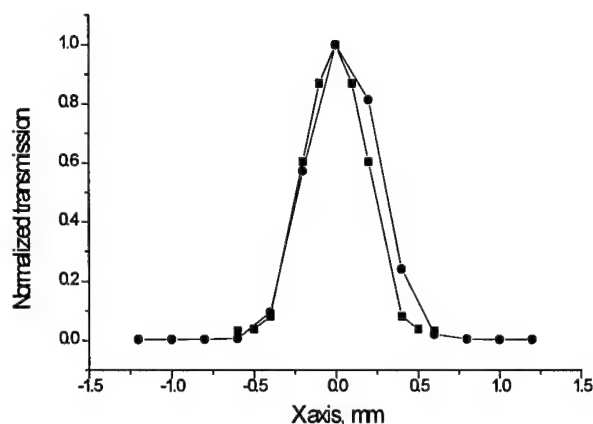


Figure 33. Transmission of a multifiber collimating lens as the source is moved transverse to the lens axis. Circles are measured data, and boxes simulation results.

mammography.

The aligned transmission measurements of Figure 27 and Figure 31 are important to determine the collection efficiency of the lens. Variation in transmission as a function of entrance angle is important for estimating the scatter rejection properties of other optics which might be used post patient. This variation was measured by first aligning the source with the lens and then moving the source in the plane transverse to the capillary axis. The transmission efficiency decreases when the x-ray source is moved off-axis because the angle between the x ray and the reflection surface of the capillary increases. Because the reflectivity decreases sharply with angle this produces greater loss at each reflection. In addition, x rays traveling through the capillary at a larger angles undergo more reflections. A comparison of measured and simulated data, with good agreement, is shown in Figure 33. Variation in the width of the scan as a function of the lens to source distance is also used as the primary method of determining both the focal distance of the lens, and the depth of field. The measured variation is plotted in Figure 32. The depth of field can also be seen in Figure 27, which shows the measured and simulated transmission as a function of source to lens distance. The depth of field is about 11 mm.

#### Divergence and Diffraction Gain

Measurements of the exit divergence of the collimating optic have been performed at 8 keV and at 20 keV. Exit divergence is important if a capillary optic is to be used as a collector fore slit before the patient.

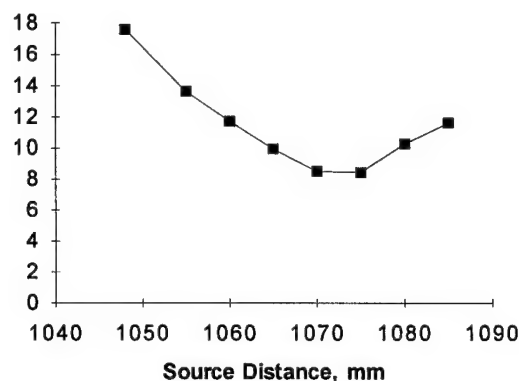


Figure 32. Width of scan of transverse source scan, as a function of source motion along the lens axis, for collimating lens, measured at 20 keV.

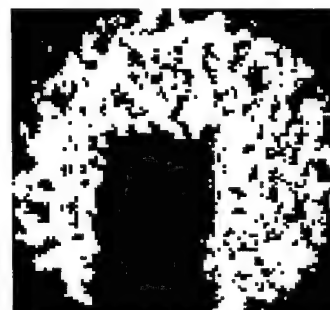


Figure 34. Image of lens shown in figure 30, taken 30 cm after the lens.

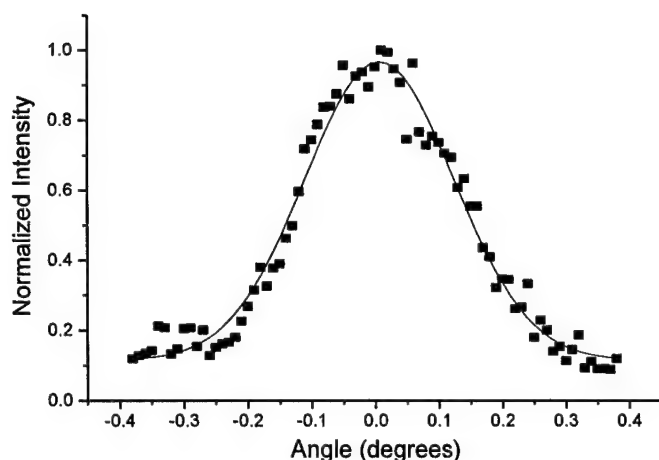


Figure 35. Output divergence of the 8 keV collimating lens, measured at 20 keV.

In this case, the spatial resolution will depend on the angular spread of x-rays at the exit end of the polycapillary fibers. Large angular divergence is equivalent to a large focal spot size in a conventional system. The divergence, measured by rotating a silicon wafer in the beam and measuring the width of the diffraction curve is shown in Figure 35. The full width of the divergence measured at 20 keV is 2.56 mrad, slightly greater than the critical angle for total external reflection. The effect of the divergence is shown in figure

34, in which the image of the fiber bundle walls have been blurred by placing the film 30 cm behind the lens.

The ability of the optic to redirect the collected x rays into a beam of relatively low divergence means that the reflection efficiency off a monochromatic crystal is greatly enhanced. While the low power test source was not intense enough to permit imaging after monochromatizing, measurements were made of crystal reflectivity. A silicon (100) crystal was found to reflect approximately .0047% of the beam from the molybdenum source after collimation. This is in reasonable agreement with a calculation<sup>18</sup> of expected reflectivity for a crystal with 0.14 mrad mosaicity, which is reasonable for the crystal used. The gain, relative to no collimation, is on the order of 100x.

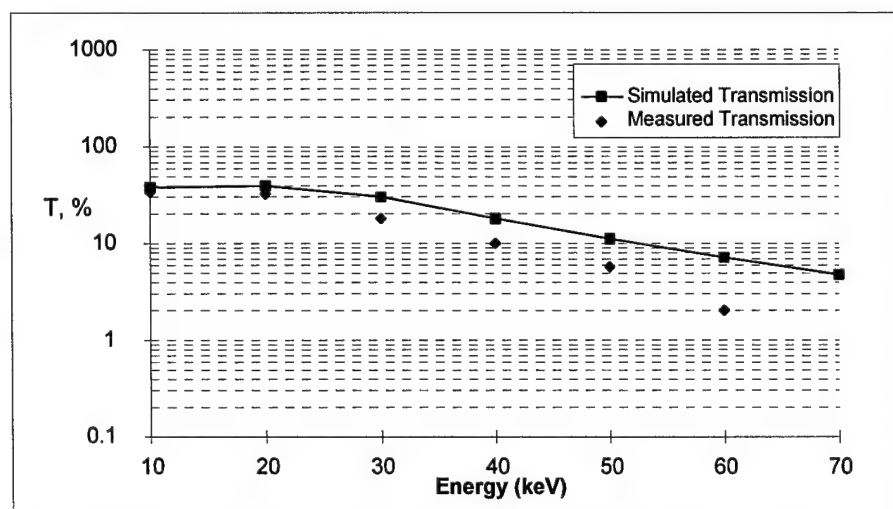


Figure 36. Simulated and measured transmission of the 20 keV prototype.

#### 20 KEV PROTOTYPE

A second collimating lens designed for higher energies was also tested. This lens has a focal length, 1m, which was longer than ideal for mammography, but a much larger transmission, in excess of 30% at 20 keV, as shown in Figure 36.

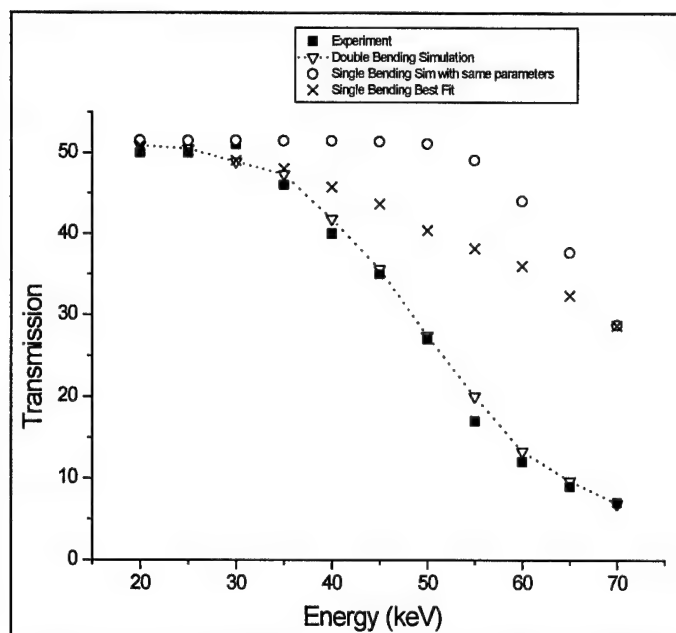


Figure 40. Transmission efficiency of a central (nominally straight) polycapillary fiber in the 20 keV prototype collimator. The fiber OD is 350  $\mu\text{m}$  and the channel diameters are 10  $\mu\text{m}$ . The fiber length is 14 cm. Simulated values are shown for a single bend and for a compound (double) bend. All of the simulation results assume a roughness  $z = 0.3 \text{ nm}$  and waviness,  $w = 0.2 \text{ mrad}$ .

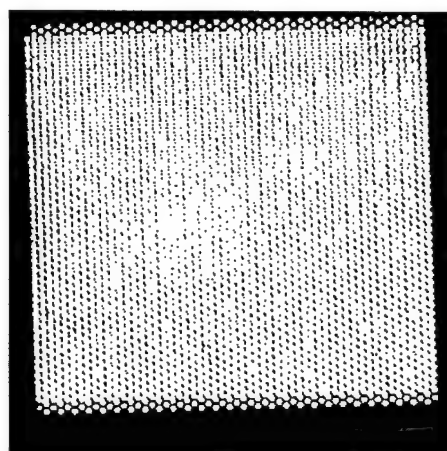


Figure 37. X-ray micrograph of 20 keV collimator, exposed 5 min at 60 keV and 0.4 mA with a W source and Polaroid film.

The drop-off at higher photon energies is due to some curvature of even the central fibers, as explored in the simulation of Figure 40. The output field was also much more uniform than for the previous collimator, as shown by the picture in

Figure 37 and the measurement of Figure 39. At lower exposure, in Figure 38, it can be seen that there were some defects in the right half of the lens. This was due to some fiber misalignment, which was reflected in the divergence measurements. This lens was a first test of a new screen technology, which has since been improved.



Figure 38. X-ray photograph of 20 keV collimator, exposed 5 min at 35 keV and 0.25 mA..

Figure 39. Output intensity distributions for the prototype TYPE I collector for different energies.

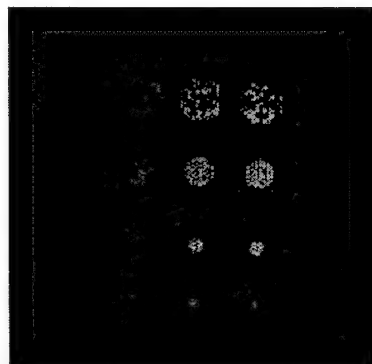


Figure 42. Polaroid film radiograph of Lucite phantom placed 5 cm from the phantom. Upper holes are 6 mm in diameter, second row is 4 mm, third, 2 mm, and fourth, 1 mm. Holes on the right are 3.5 cm deep, middle holes are 3 cm deep and holes on left are 2 cm deep.

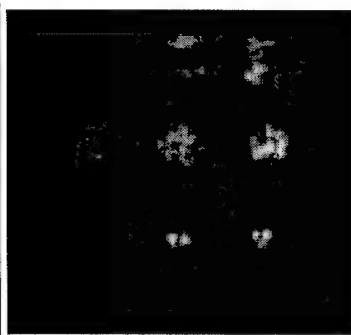


Figure 41. Polaroid film radiograph 95 cm from the phantom.

and very low exposure the image is reasonably clear. The images were taken with normal, x-ray insensitive Polaroid film and a very low power, 0.20 mA test source. In both cases the phantom was placed close to the output of the lens.

Preliminary imaging measurements have been performed with the optic. Figure 42 and Figure 41 are radiographs of a 5 cm thick Lucite phantom. Figure 42 was taken with the film 5 cm from the phantom. Figure 41 was taken with the film 95 cm from the phantom. There is no magnification for this parallel beam geometry. However, some blurring due to fiber misalignment is observable. Given the long distance, known fiber misalignment

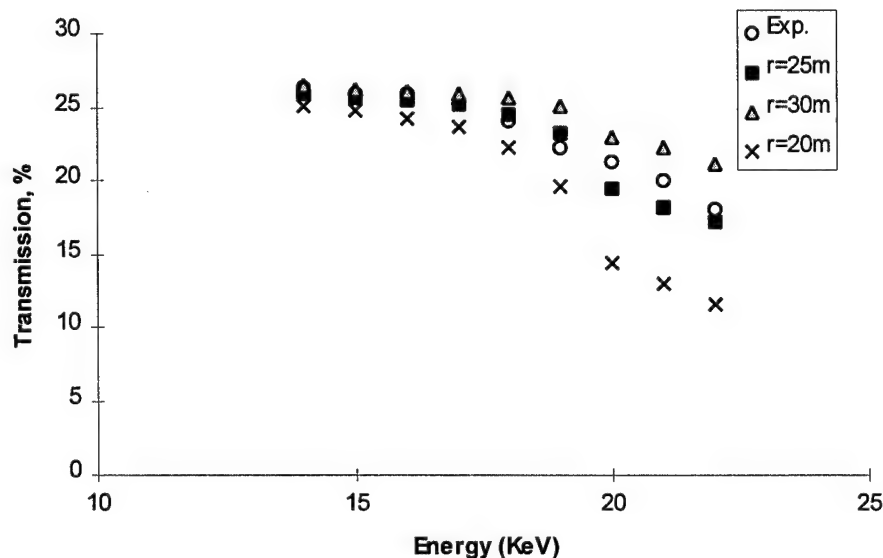


Figure 43. Simulation of straight antiscatter lens, compared to measured data. Simulation uses 1 nm roughness, 0.45 mrad waviness, and 26% overall open area.

### Anti-Scatter Optics

#### STRAIGHT MULTIFIBER OPTIC

Rather than simply using long air gaps to eliminate scatter, as in Figure 41, a straight polycapillary antiscatter optic could be employed, as shown in Figure 26. Such an anti-scatter optic, which was essentially a 3 cm diameter bundle of straight polycapillary fibers, was aligned to the output of the 8 keV collimating lens. The anti-scatter optic was 150 mm in length with 55μm channels. The

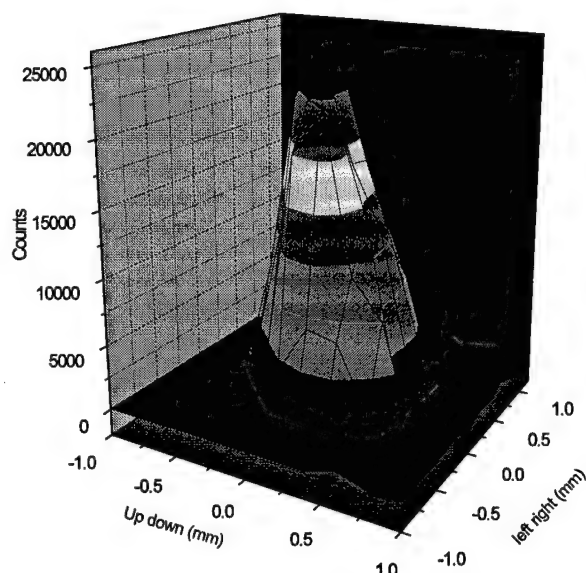


Figure 45. 2-D source scan of early prototype optic (input diameter = 2 mm, output diameter = 3 mm, transmission = 5 % at 20 keV, focal distance 22 cm) This lens transmits poorly because only the central capillary channels transmit while the outer capillaries do not transmit at all. Only about 33 % of the optic cross section transmits at 5 % or greater.

transmission spectrum of this optic is

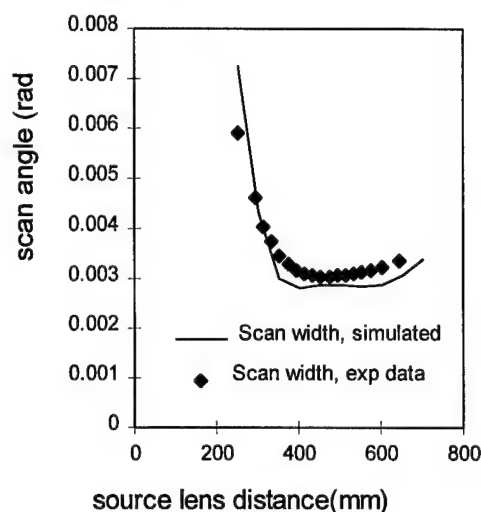


Figure 44. Source scan of tapered lens.

shown in Figure 43. Simulations show that the apparently straight fibers have significant curvature, with radius of curvature of about 25 m.

#### MAGNIFYING LINEAR MONOLITHIC OPTICS

Linear monolithic optics taper as a single glass unit from input to output as shown in Figure 2 and Figure 46. These optics are relatively difficult to manufacture. Many early prototypes have poor transmission, as shown in Figure 45. To help

#### Scanning Geometry

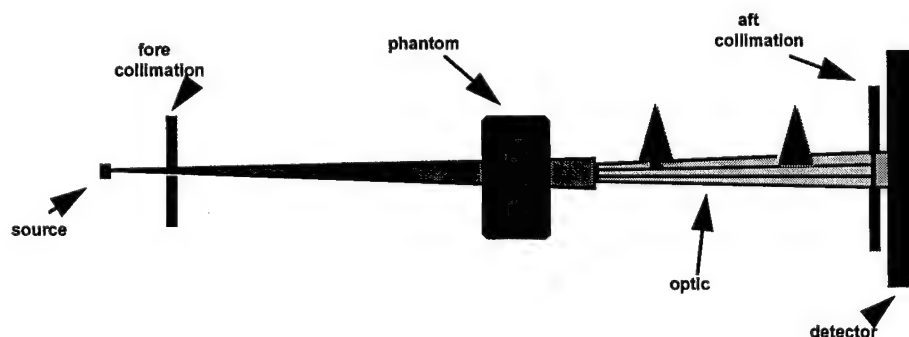


Figure 46. Small optic scanning geometry for contrast and imaging measurements.

understand the defect problem an extensive simulation and measurement study was performed on one of the better prototypes.

The focal distance of a polycapillary optic can be determined by



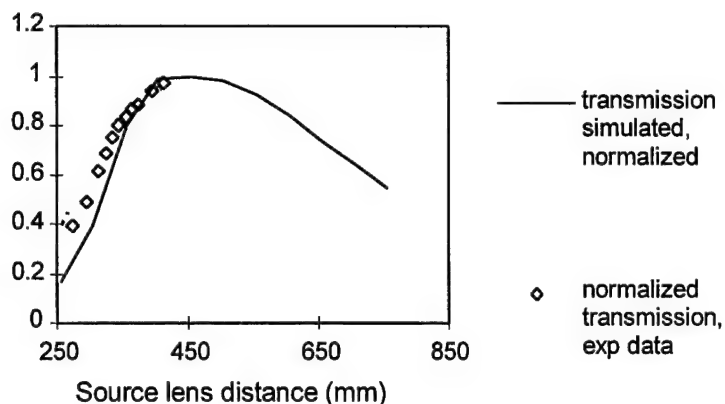


Figure 47. Transmission of tapered lens.

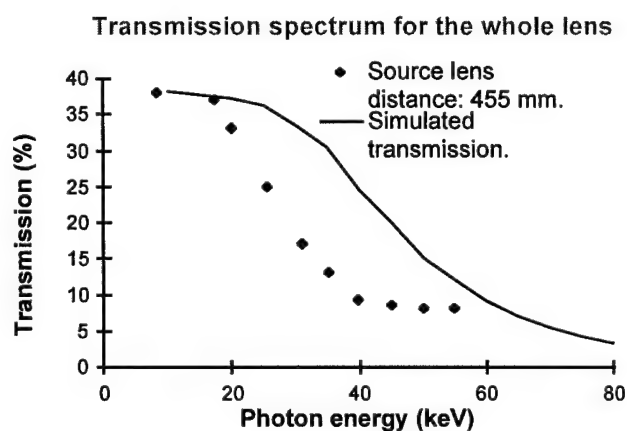


Figure 48. Transmission of whole tapered lens.

widths have to be measured very carefully to determine the focal distance. The focal distance determined by minimizing the scan angle is 455 mm for this lens. Transmission and photon counts are also plotted versus source lens distance in Figure 47 along with the simulation values. The maximum point for transmission is around 450 mm. The second method can be affected by the source instability.

Transmission was measured in a wide energy range for the whole lens as well as the central part of the lens. The transmission spectrum for the whole lens is plotted in Figure 48. The figure shows that the transmission drops quickly for photons with energy higher than 20 keV, but the transmission under 20 keV is almost flat. The low transmission in the high energy range can be explained by the non-linearity of the lens. The outermost channels are more bent

finding the smallest scan angle or the maximum transmission. Source scan curves in both x (horizontal) and y (vertical) directions were recorded after the source and the lens were in alignment. FWHM of the scan curves in both directions are calculated with Gaussian fitting, and the average FWHM is taken as the scan width at that position. Scan angle is defined as the result of the average scan width

divided by the source-lens distance. In Figure 44, scan angle is plotted as a function of source lens distance. Since the theoretical curve does not have as many data points as the experimental curve, it is not as smooth as the experimental curve. This method is not effected by the source instability, and hence is very useful when the experiment needs a long time, and the source is not stable. However the curve is quite flat near the focal distance, as expected by simulation. The scan

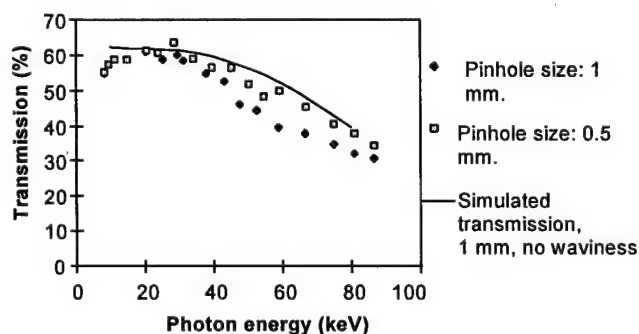


Figure 49. Transmission of the central part of the tapered optic.

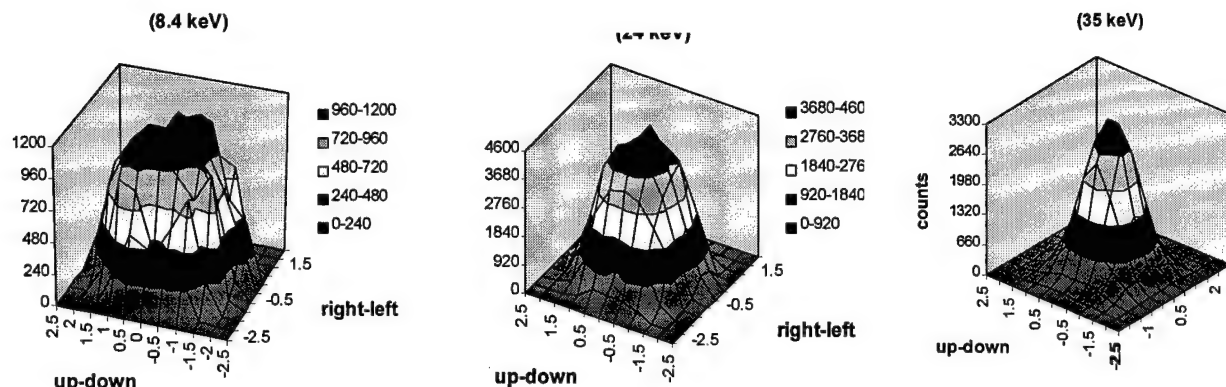


Figure 51. Two dimensional scans of the output of the tapered optic.

than the central channels, so they have low or zero transmission at the higher photon energies. This is confirmed by the higher transmission measurement at the central part of the lens, shown in Figure 49 and the transmission uniformity measurement at different energies, shown in Figure 51. Transmission uniformity of the lens was measured by putting a 200  $\mu\text{m}$  pinhole in front of the lens and performing a two dimensional scan. At 8 keV, the whole lens transmits, although we can see the transmission is not completely flat due to the non-linearity and the defects of the lens, such as blocked channels. At 25 keV, transmission of the whole lens drops to 25%. Most of the lens is still transmitting at 25 keV, but the outer channels have lower transmission than the central part. At 35 keV, the lens has a narrower transmitting region. The measurements show that the lens has undesirable nonlinearity.

Studies were performed on another optic to investigate the distributions of defects which diminish transmission. A poorly transmitting optic was cut into two pieces. The transmission of each piece is shown in figure 50. The transmission of the pieces compared to the original is shown in figure 52. This work is ongoing.

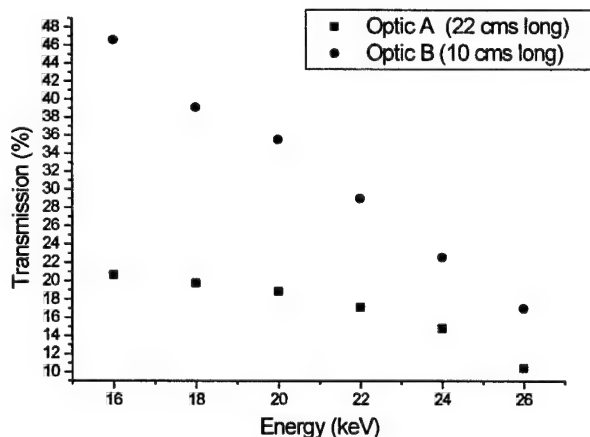


Figure 50. Transmission of two pieces of a tapered optic.

Simulations plotted in Figure 47 and Figure 48 as the solid lines assume when the lens is uniformly bent. The simulations used the same roughness and waviness correction as that used for fiber D in Figure 5. A linear tapered lens is ideal for mammography, because, as shown above, any curvature can cause transmission reductions. However, the lens currently available has a nonlinear profile. The profile is not circular, but to simplify the simulation, we assume



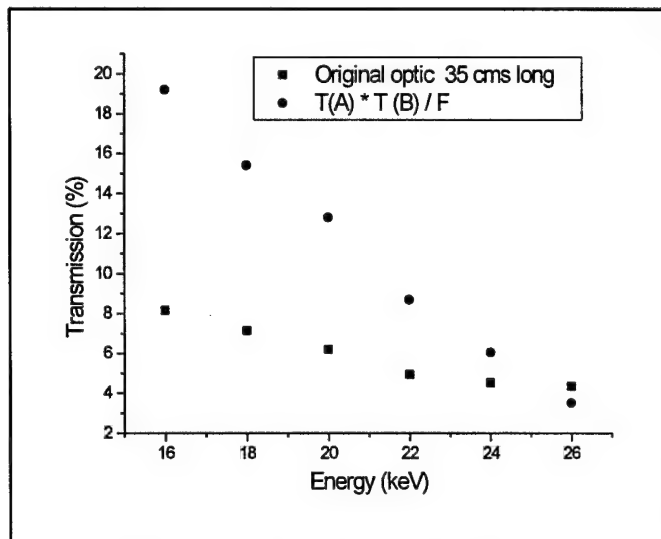


Figure 52. Transmission of original optic compared to two pieces.

that the profile is circular. A uniform bending will provide the best transmission performance for a given bending angle, so the simulation will overestimate the lens performance. A further simplification assumes the lens has a fixed channel size, although the channels actually taper with the lens. A more sophisticated lens simulation program is under development.

The geometry for uniformly bent nonlinear lenses is shown in Figure 53. The simulation method for a uniformly bent lens is an extension of the simulation for uniformly bent polycapillary fibers.

The simulation is done by sampling channels in the input cross section of the lens with an even step size. In the simulation for a bent fiber it is assumed that the capillary bends in -y direction, and z direction is along the input axis of the fiber. In order to reuse the old simulation code, the coordinate of the simulation x-y-z is rotated to x'-y'-z', where z' is the direction of channel axis at the input end and -y' is the channel bending direction. Assume the source position and the capillary position at input end is  $(x_s, y_s, z_s)$  and  $(0, 0, z_i)$  respectively, then the source capillary distance is  $z_i - z_s$ . The origin of the coordinate is selected to be the focus point of the lens.

Another parameter needed by the simulation is the bending curvature of the selected channel. This value varies with the position of the channel. The calculation of the bending curvature is demonstrated in Figure 54.

First it is assumed that the channels are evenly distributed on both input and output cross section. Let input and output diameter of the lens be  $r_i$  and  $r_o$ , and focal distance  $\overline{OA}$  be  $f$ , and the lens length  $\overline{AC}$  be  $L$ , then

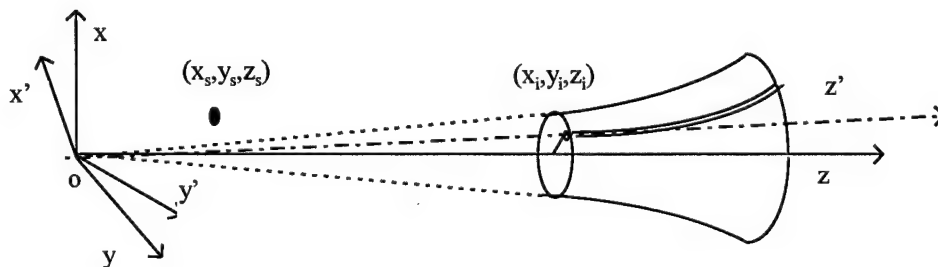


Figure 53. Geometry for Lens simulation.

$$\overline{AB} = \sqrt{x_i^2 + y_i^2}, \quad \overline{CE} = \overline{AB} * r_o / r_i$$

$$f / (f + L) = \overline{AB} / \overline{CD}, \quad d = \overline{CE} - \overline{CD}$$

For a small bending angle,

$$\alpha \approx L / R = d / (L / 2)$$

where R is the bending radius, d is the distance between point D and E as shown in Figure 54, and  $\alpha$  is the bending angle. Thus

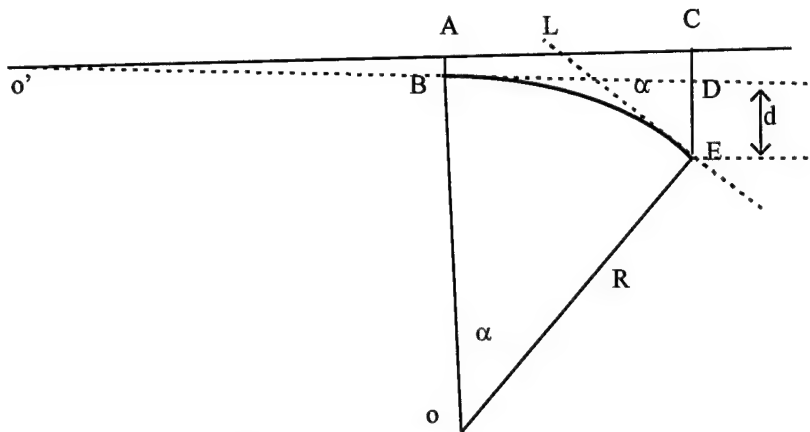


Figure 54. Curvature estimation for lens simulation.

$$R = L^2 / 2d \quad (1)$$

The simulated results in both cases show higher transmission than the experimental results. This indicates that the lens has more reduction in transmission due to the bending. This is expected, because the lens does not have a uniform bending.

#### Manufacturing Issues

The only practical method to produce larger linear tapered anti scatter optics is to couple several smaller optics together to form one large optical component. The method we propose to attach the individual optical elements together is quite similar to the method that is used by the company to align polycapillary fibers. These multifiber devices consist of thousands of individual polycapillary fibers that are strung through rigid grids to produce a single large optic. The individual fibers must be aligned to within a few microns in position and to less than a milliradian in angular orientation. These requirements are more stringent than those required in this project. The alignment technology is not likely to be a problem. However, first high quality monolithic tapers must be reproducibly manufactured.

XOS has developed the capability to make long tapers with diameters up to 5 mm with transmission which indicate the future potential, but which is currently less than half the expected value. Work is necessary to improve profile control (linearity), increase transmission efficiency, and increase achievable optic diameter. Single examples have been manufactured which demonstrates sufficiently good performance to support the medical imaging research and demonstrate the feasibility of the

approach. However, considerable work is necessary to achieve optics suitable for clinical use.

There has been substantial progress in achieving the necessary manufacturing control to repeatably produce high quality optics. The manufacturing technique was carefully studied, the critical problems were identified, and a plan was prepared to modify the manufacturing process. The first step was to increase the controllability and reproducibility of the manufacturing process. The development of monitoring automation and feedback systems was achieved. As a result of the improvement in process control, systematic and rapid improvement has been made in the development and manufacturing of new optics.

Initially, glass preforms and prototype optics were produced in Russia. They were of relatively poor quality, and no two optics were equivalent in performance, but

Table 3

PROBLEMS	ACTION NECESSARY
<ul style="list-style-type: none"> <li>decrease in open area</li> </ul>	<ul style="list-style-type: none"> <li>better temperature profile control</li> <li>better tension control</li> <li>evaluate tension - temperature trade off</li> </ul>
<ul style="list-style-type: none"> <li>inclusions, primarily glass particles</li> </ul>	<ul style="list-style-type: none"> <li>improved handling and bundle assembly procedures</li> <li>static electricity abatement including controlling for humidity</li> <li>laminar flow hoods</li> </ul>
<ul style="list-style-type: none"> <li>cast (curvature)</li> </ul>	<ul style="list-style-type: none"> <li>improved alignment of feed mechanism, furnace, and puller</li> <li>radially symmetric uniformity of heat zone</li> <li>longer cooling zone</li> <li>better control of air flow</li> </ul>
<ul style="list-style-type: none"> <li>OD control</li> </ul>	<ul style="list-style-type: none"> <li>improved temperature and tension control</li> <li>real time monitoring of OD with closed loop feedback</li> </ul>
<ul style="list-style-type: none"> <li>waviness in glass surface</li> </ul>	<ul style="list-style-type: none"> <li>elimination of internal vibration sources, e.g., friction, motors being operated slower than designed, turbulent forced air cooling</li> <li>isolate from external vibration sources</li> <li>change to cutter approach which doesn't cause large periodic shocks</li> <li>more homogenous glass (optical quality)</li> </ul>

they served as proof-of-principle devices. Because of the technical and political difficulties, Russian optics and preforms are no longer available. When it became apparent that having the optics manufactured in Russia was not viable long term, X-Ray Optical Systems, Inc. (XOS) commenced developing a U.S. manufacturing capability.

XOS chose to work with the polycapillary subcontractor that has the best controlled process for making polycapillaries which work well at 8 keV. The glass is formed by a continuous, steady state, vertical pulling process, with as much as 1,000 meters in a single production run. Several manufacturing runs were conducted with evaluations of the polycapillaries done between each run. Adjustments to the process were made for each new run. XOS personnel participated in some of the runs. The polycapillary performance and the manufacturing process were carefully analyzed to determine what changes were needed in manufacturing to obtain the desired polycapillary capabilities. This manufacturer does not use computer control. There was no automatic feedback in the manufacturing system. The system was controlled by having an operator observe that a condition such as the outer diameter of the polycapillary or the furnace temperature had drifted from the desired point and then manually adjusting one of the control variables. The polycapillary performance at high energies was not acceptable. Problems which were identified, and the actions determined to be necessary are identified in the Table 3. XOS determined that this supplier was not able and/or willing to make the necessary equipment, personnel, and operational changes. With this information, XOS modified an in-house glass pulling system to investigate the effect of making some of the changes which were determined to be necessary.

A systematic evaluation the major manufacturing parameters was not possible initially as the first prototypes made were pulled on a setup where there was little control over the manufacturing parameters, and little ability to record the parameters during the forming process. The initial setup was put together inexpensively to provide some indication of the direction to proceed. It enabled a definition of a general range for some of the manufacturing parameters, such as pulling speed, so that acquired information could be used to design a more sophisticated pulling setup. One source of variation in the prototype monolithic optics came from the uncontrolled air flow through the furnace.

Modeling of the optic shaping process was conducted. Modeling provides some understanding of the underlying relationships between the manufacturing parameters and the resulting optic. Constant feedback of the experimental results to increase the accuracy of the model is an important input to the scientific, quality, and production methods. The modeling is based on a one-dimensional finite-differences algorithm. The preform (large outside diameter polycapillary bundle) is split into finite elements. This approach allows the thermal and mechanical properties of each segment to be calculated. At each time step, the ends of the preform are moved according to a predetermined, but likely variable, speed. The formation of the lens occurs in the heated area and the glass will flow according to viscosities. Since the total volume of each element is kept the same, the elements that are stretched the most end up with the smallest diameter. The radiative heating by the furnace as well as radiative cooling

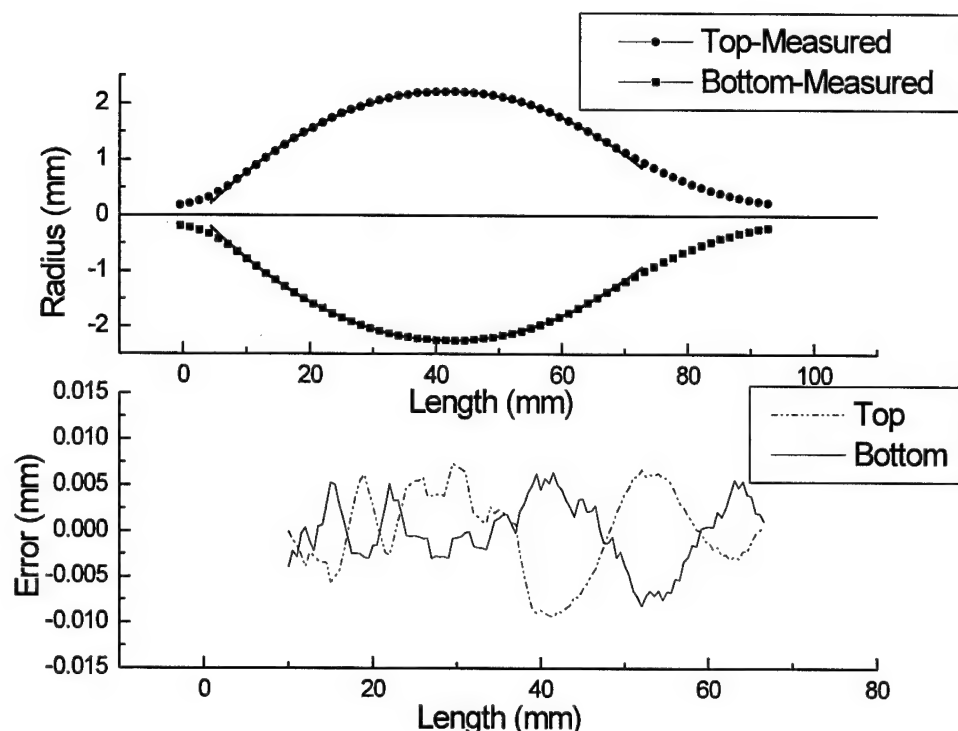


Figure 55. Variation in optic profile, compared to design.

from the preform must be considered. The thermal profile for the preform can be calculated for points along the center axis of the furnace.

A second generation pulling tower was constructed and instrumented to allow flexibility in controlling different parameters and to record the actual status of parameters during the pulling. The tower uses servo motors with encoders to displace the preform and furnace; multiple thermocouples to monitor the temperatures; and load cells to monitor the pulling forces. So far a few long tapered monolithic optics have been formed using this system. There are numerous independent and dependent variables that effect the quality and reproducibility of a lens design. In addition to the parameters already known to effect the reproducibility and quality of the lens, it is expected that others will be revealed. An important part of the project will be to establish the relative importance of each parameter through a systematic, multivariable experimental approach. The goal being to seek a rapid high-quality path to large tapered monolithic polycapillary lens production. Several of the development steps will proceed concurrently. An example of this is the storage, treatment, and holding methods of the preforms can be investigated while the lens formation process is proceeding through its initial data collection and analysis steps. Although the ultimate quality of the lens is dependent on each of these paths, the synergism is likely not realized until the relative significance of the basics is established. The preform material will be characterized for open area, x-ray transmission, uniformity of outside diameter.

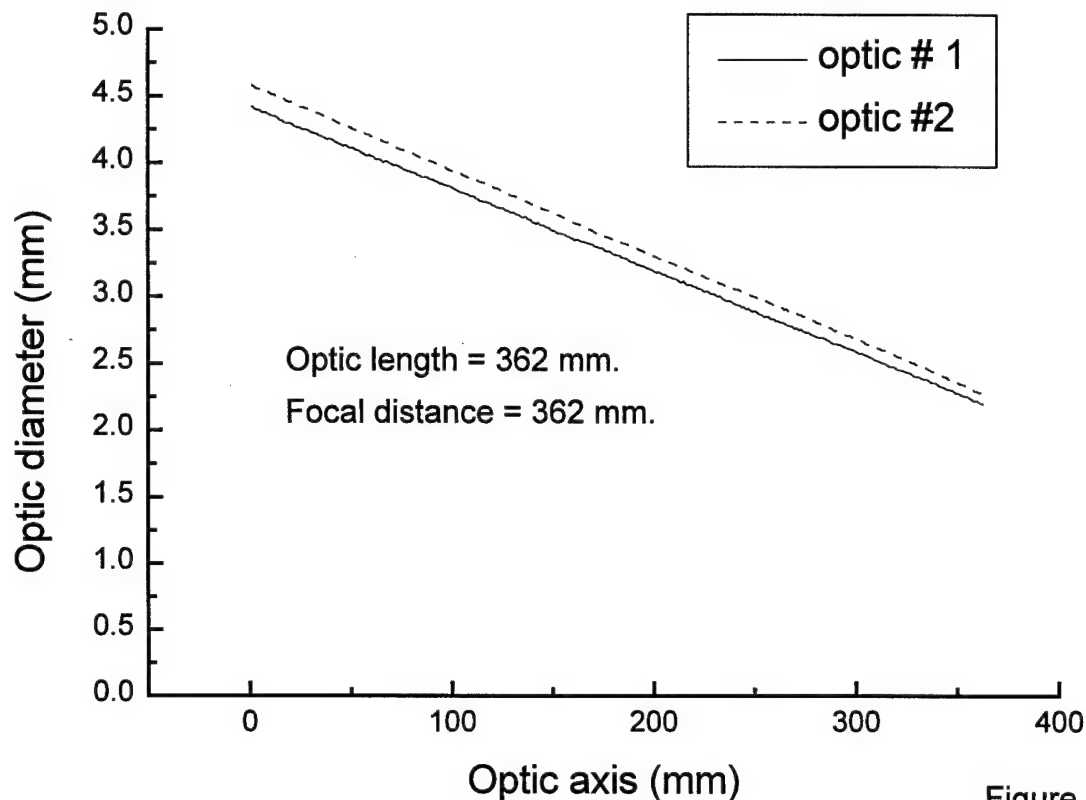


Figure 1

Figure 56. Profiles of two recently manufactured matched linear tapers.

General observations of the presence of inclusions, cleanliness, and uniformity of color will be noted. Then the appropriate method of storage prior to use needs to be investigated. Precautions to protect the material from dust and moisture will be taken.

There is a strong interdependence of tension on the preform, temperature in the various heating zones, speed of the pull, and mechanical feedback. Extensive correlation of the data from the forming process with the lens performance will be needed to optimize the system. Additional considerations include the heat capacity of the glass and time-temperature response of the furnace. Uniformity of gas flow through and around the glass during the pulling step is important to monitor. To assure uniformity and appropriate use of heat zones, other parameters to consider include: baffling, furnace diameter, and correlation of furnace motion with the movement (i.e. flow) of the preform. In a motor driven system, there are vibrations, motor inertia, slew rates, as well as bearing, slide, and belt qualities that must be evaluated. Other mechanical conditions to evaluate include how the preforms are held and supported to maintain uniform alignment and minimize random and systematic perturbations. Despite the number of parameters to be considered, only a few are thought to be critical to first order, others affect the quality in diminishing amounts. In fact, most will not become an



Figure 57. X-ray transmission image of linear taper shown in figure 56.

issue of concern until the grosser variable are better controlled. Fairly early in the process, XOS has made significant progress in the design and construction of monolithic polycapillary optics.

The first example is a set of 17 keV focusing optics designed for microfluorescence analysis. The profile of the optic was measured with a microscope-based MicroVu video coordinate measuring system at XOS. The precision of the system is about 5  $\mu\text{m}$ . Figure 55 shows the measured profile compared with the design profile. Deviations along the optic axis between the two profiles are also shown in Figure 55. More recently, two very well matched magnifying linear tapers were produced for placing in a multi-taper jig. The

profiles of the two optics are shown in Figure 56. Although the optic profiles are excellent, x-ray transmission efficiencies of all four optics fabricated so far are pretty bad (less than 10%). Based on x-ray characterization on both original bundles and long linear tapers, we conclude that the poor x-ray transmission is due to randomly distributed defects in the original bundles. Figure 57 shows an x-ray image of the linear taper, showing some areas of poor transmission.

#### Imaging Measurements

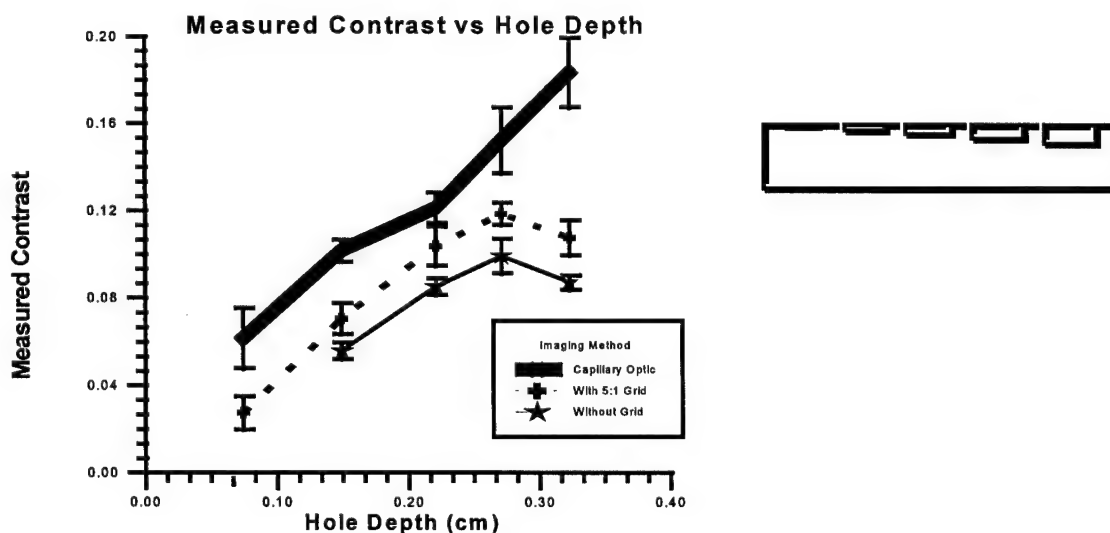


Figure 58. Contrast enhancement measured for a small scanned capillary optics using a phantom consisting of a Lucite block with drilled holes.





Figure 59. Image of contrast phantom made with scanned optic.

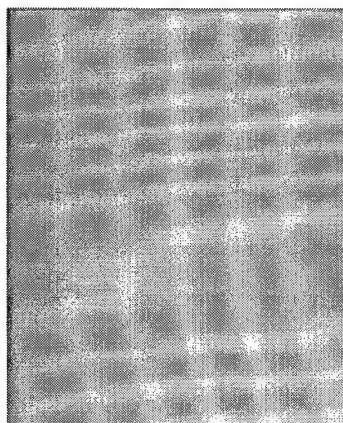


Figure 60. Image of contrast phantom produced with conventional grid.

An image made with a scanned optic and with a conventional grid are shown in Figure 59 and Figure 60. Improvements have been made in the scanning system to reduce image artifacts. Scan lines which were visible in previous images are not apparent in Figure 59.

The optic was also used to measure the resolution enhancement due to magnification. A plot of the measured MTF is shown in Figure 61. At the 0.1 MTF level, the resolution improved from 4.5 lp/mm<sup>2</sup> without the optic to 8.9 lp/mm<sup>2</sup> with the optic. The MTF of the very linear optic from Figure 56 is shown in Figure 64. It shows nearly ideal performance despite the low transmission.

### Artifact Reduction

Modulation Transfer Function (MTF) is the most fundamental measurement of spatial resolution used in radiology. The standard technique is to image a slit, determine the line spread function (LSF), and compute the Fourier transform. The MTF measured for the mammography system with capillary optics, compared to that without

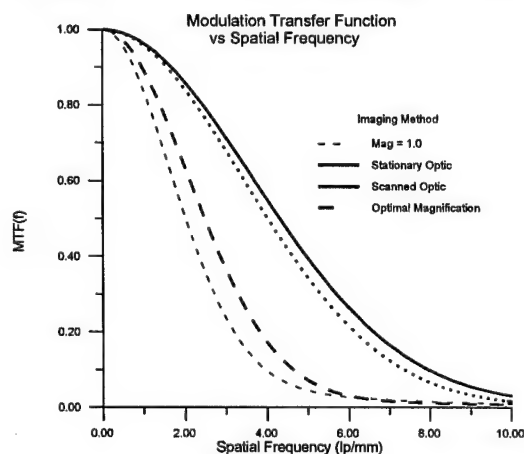


Figure 61. Modulation transfer function.

the capillary optics, will give the resolution improvement and also can be used to diagnose artifacts. For some lenses, the transmission is not always uniform, as shown in figure 62, which is an image of the output from a lens.

The structure of the capillary bundles was obvious. In this case, the LSF could not be obtained by imaging a slit without background elimination. The background deducted slit image is the slit image divided by the image with capillary only. However, this involves image registration. The information for background that can be used for image registration is too little in the slit

Contrast enhancement measurements have been performed with a small scale (2 mm diameter) optic as part of an on-going collaboration with the Univ. of Wisconsin.<sup>19</sup> The geometry for the scan is shown in Figure 46, and the resulting contrast enhancement compared to the no optic and conventional grid cases are shown in Figure 58.



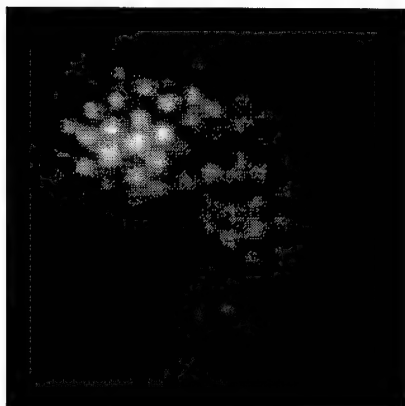


Figure 63. Magnified image of the background with lens structure.

image. An alternative method is

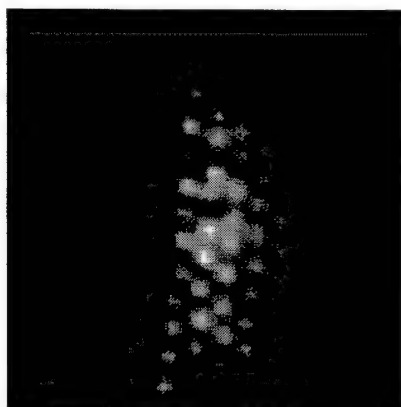


Figure 62. Magnified image of a lead edge. Real image size: 5(mm) X 5(mm).

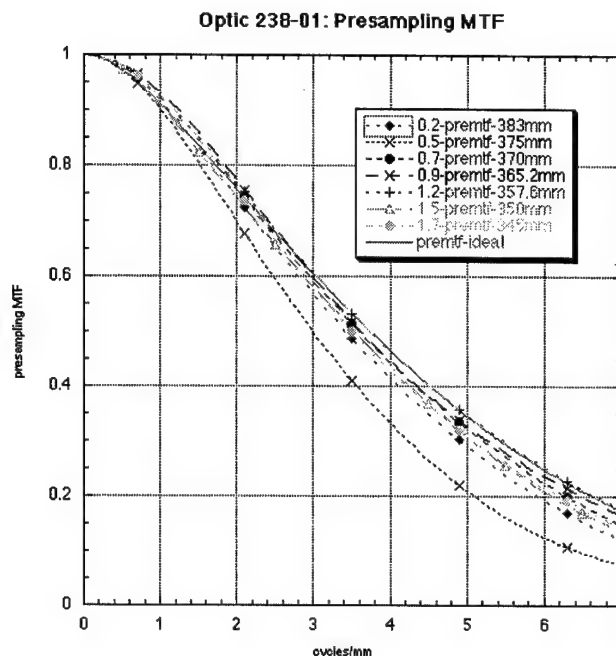


Figure 64. MTF of newest, most linear taper at different source to optic distances. MTF is nearly ideal.

calculating the LSF as the derivation of the edge spread function (ESF). The edge image left enough background for registration so that it could be a feasible method in our case.

A registration algorithm (FMI-SPOMF) proposed by Chen, et al.<sup>20</sup> was used in this work. This is a method to match a two-dimensional image to a translated, rotated and scaled image. The approach consists two steps: the calculation of a Fourier-Mellin Invariant (FMI) descriptor for each image to be matched, and then matching of the FMI descriptors. FMI descriptors are translation invariant. The matching of the FMI descriptors is to find out the rotation and scaling, and achieved using a symmetric phase-only matched filtering (SPOMF). In our case, there is no change in scaling, but rotation is probably involved. When the rotation was found, image translation is found by SPOMF method.

Images with and without edge are shown in Figure 62. and Figure 63. The edge was made of a lead plate. The size of each image is fifty by fifty in pixels. They were taken in an experimental digital mammography system with a computed radiography digital phosphor plate. The digital CR plate has limited resolution, 5 lp/mm, and is usually considered to be not good enough for clinical mammography. But the effective resolution of the system could be improved by the magnification of the capillary optics.

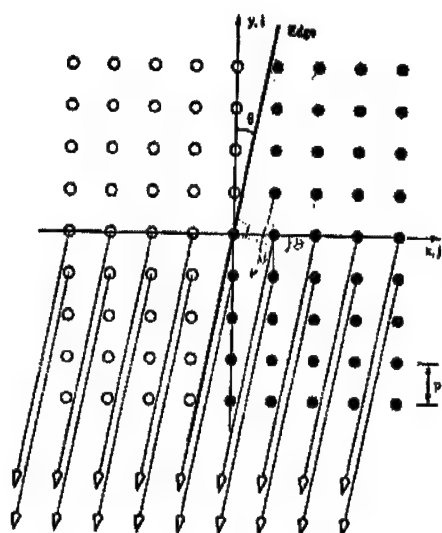


Figure 66. Reprojection of a two-dimensional edge image into a finely sampled ESF.

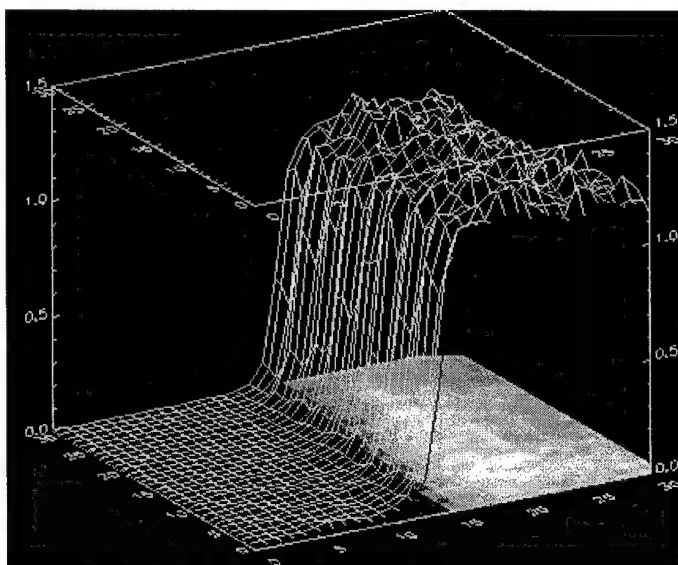


Figure 65 Three-dimensional edge image after background subtraction.

The magnification of the capillary lens used in the system is 1.86, so that the effective resolution should be improved by a factor of 1.86. The registration algorithm was implemented in IDL. With the FMI-SPOMF registration algorithm, no rotation was found. The translation was then found by SPOMF algorithm. The difference between the usual correlation method and SPOMF method is that it only uses the phase information. The phase-only correlation function has sharper peak than normal correlation function. Sub-pixel resolution could be achieved theoretically. However it was found that the resolution is not good enough in our case. This may be caused by the relatively small image size. The background-subtracted result was further optimized by manual shifts in sub-pixel range. The result after manual optimization was shown in Figure 65. The periodic background is totally gone. A cubic spline interpolation method was used for the best result while shifting the background image relative to the edge image.

The presampling MTF includes unsharpness of the detector and the sampling aperture. In order to eliminate the aliasing, a finely sampled ESF is obtained with a slightly angulated edge in a single exposure as illustrated in Figure 66.<sup>21,22</sup> The angle in our edge image in Figure 65 was calculated to be around  $6^\circ$ . The resultant ESF is plotted in Figure 67. A direct calculation of MTF is to take the derivation of the ESF and result a LSF, then take Fourier transform. As it can be seen, the ESF in our case is not smooth enough for a direct calculation. An alternative technique is to use an ESF fitting procedure.<sup>23</sup> In the fitting method, the ESF is represented with a term  $(1-\exp)$  and an error function ( $\text{erf}$ ) as in equation (1). MTF is calculated by equation (2), where  $a$ ,  $b$ ,  $c$  and  $d$  are fitting parameters from equation (1). The fitting curve is plotted in Figure 67 as the solid line.

$$ESF(x) = a\{1 - \exp(-b |x - x_0|)\} + c \cdot \text{erf}(d^{1/2} |x - x_0|) \quad (1)$$

$$MTF(f) = \frac{c \cdot \exp(-\pi^2 f^2 / d) + a(1 + 4\pi^2 f^2 / b^2)^{-1}}{(c + a)} \quad (2)$$

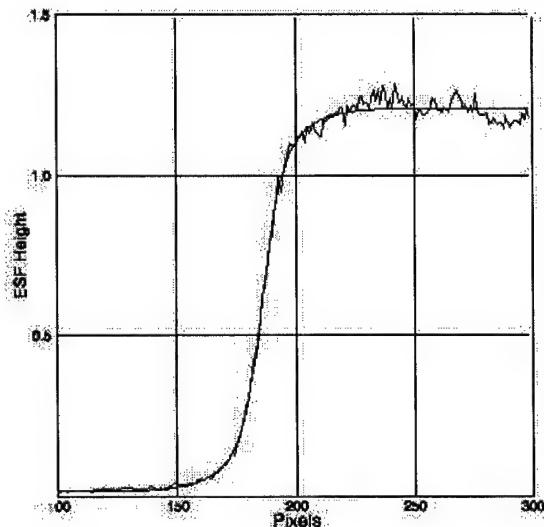


Figure 67 Edge spread function and its fitting curve.

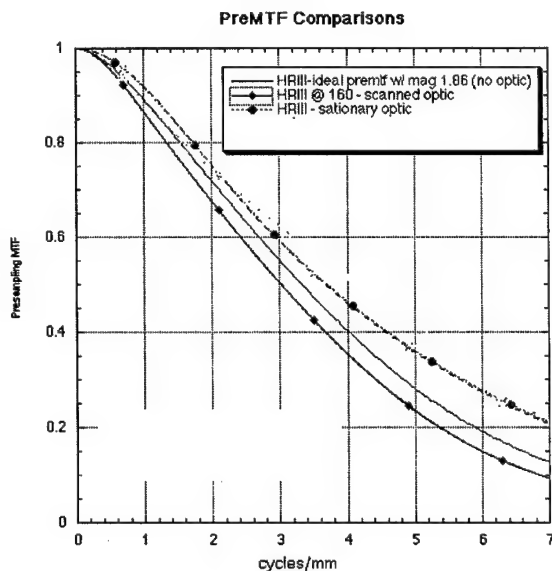


Figure 68 Calculated MTF compared with the MTFs with scan optics, and without optics.

The calculated MTF was compared with that from scanned optics in Figure 68. The MTF from scanned optics was calculated from a slit image. Optic structure was smeared out with scanning, so no background deduction is necessary. An ideal MTF was also plotted in Figure 68. An ideal MTF is the one when we assume the lens does not introduce only the 1.86 factor magnification and no image degradation. It is measured with a slit image without optics, and its result was multiplied by the magnification of the capillary lens. The measured MTF with lens should no better than the ideal MTF. However, for some reason, the MTF for stationary lens is better than the ideal MTF. It is possible that the background elimination process failed the MTF measurement. Another possibility is that the magnification of the lens is different from 1.86, since the magnification was measured separately at a different time. More experiments, necessary to determine the cause of the disagreement, are underway.

#### Demagnifying, Focusing Monolithic Optics

Monolithic optics similar to the collimating optic shown in can be used to minify an x-ray beam. Some characterization of such optics has been performed. The first measurement characterized an optic using a point source, a micro-focused transmission x-ray source (spot diameter about 5  $\mu\text{m}$ ) modified from an old SEM. Anode materials made of Cu and Mo are coated on a thin Be vacuum window. An energy-sensitive Amptek detector with an energy

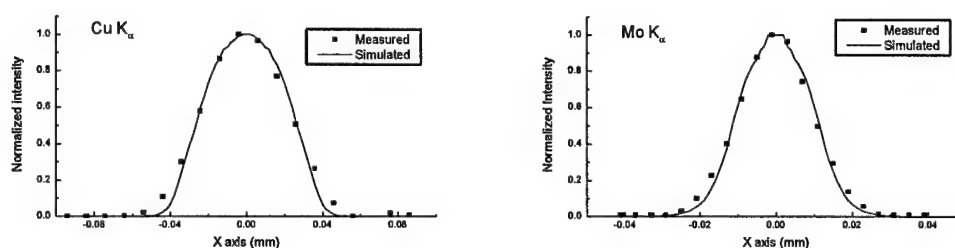


Figure 70. Focal spot scans of focusing optic.

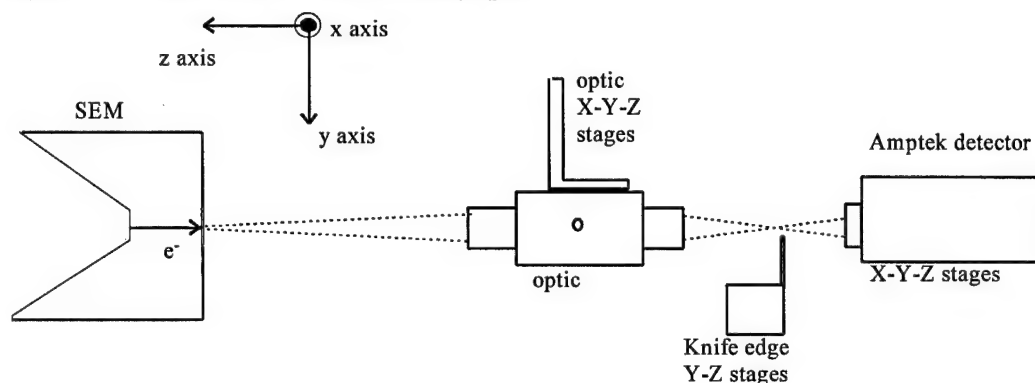


Figure 69. Schematic of the experimental setup for optic characterization.

resolution of 250 eV at 5.9 keV was used for x-ray detection. The crystal size of the detector is 7 mm<sup>2</sup>. The detector was placed roughly at the output focal plane of the optic, 8.5 mm away from the exit of the optic, to allow the detection of the output beam from the entire optic. The polycapillary focusing optic and detector were mounted on x-y-z stages which allows precise alignments among the source, optic, and detector. Figure 69 shows the schematic of the experimental setup. The alignment of the optic

input focus to the source is achieved by moving the optic in all three orthogonal directions until the transmitted flux is maximized.

The output focal spot of the prototype optic was at Cu K $\alpha$  and Mo K $\alpha$ . The measurement was performed by scanning a tungsten knife edge plate across the focused beam on the focal plane. The first derivative of the measured intensity as a function of the position of the knife edge gives the intensity distribution of the focused beam. This is shown in Figure 70, with the simulation results as comparisons. Good agreement between the measurements and the simulations indicate good alignment of the

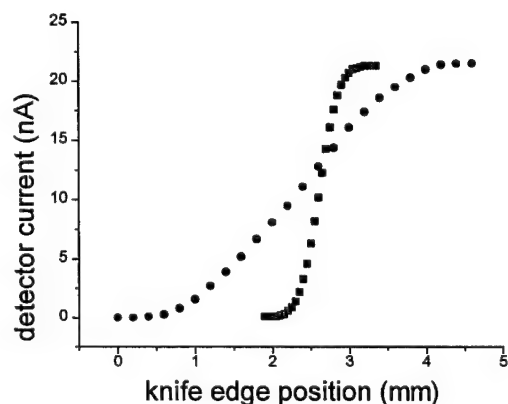


Figure 71. Knife edge scan at a knife edge to source scan distance of 103.5 (●) and 123.5 mm (■).

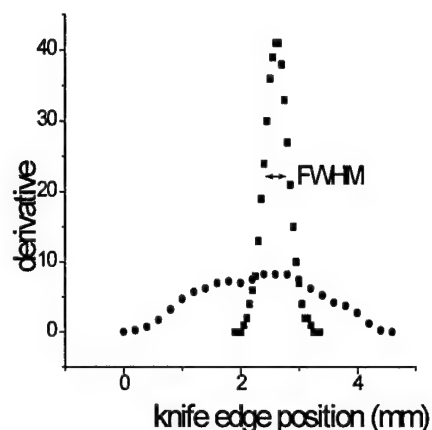


Figure 73. Derivative of knife edge scan for optic to knife edge distances of 103.5 mm (●) and 123.5 mm (■).

capillaries toward the output focus and that the simulation can reliably predict the divergence of the output beams from the capillaries. The measured spot sizes (FWHM) are 44  $\mu\text{m}$  for Cu  $K_\alpha$  and 21  $\mu\text{m}$  for Mo  $K_\alpha$ , respectively.

A second set of measurements were performed at beamline X23A3 at the National Synchrotron Light Source (NSLS) at Brookhaven National Laboratory (BNL). This is a white beam bending magnet line with a maximum white beam flux of approximately 13 W/cm<sup>2</sup>. The size of the beam could be adjusted by two sets of collimating slits. The optic was mounted on a precision motion controlled four axis stage (up-down, left-right, tilt, and rotate).. A knife edge or pinhole, mounted on another precision stage (left-right, forward-backward), could be placed between optic and the ion chamber. A small portable laser was used for rough alignment of the optics with the beam.

The spot size and also the focal distance were measured using a knife edge that was scanned horizontally across the beam. Two scans, one near to the focal

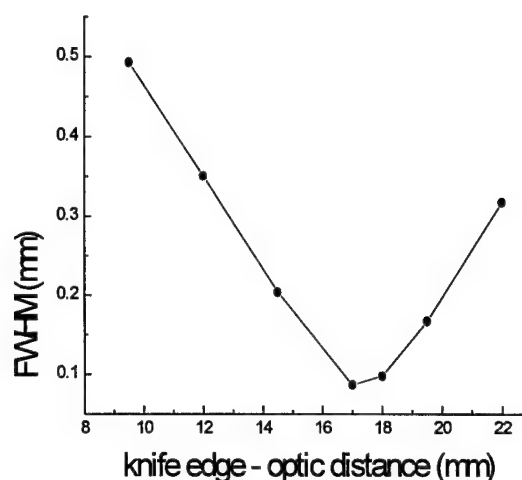


Figure 72. Width of derivative of knife-edge scan versus distance to optic for monolithic optic.

Table 4. Results for monolithic focusing optic.

X-Ray Energy (keV)	Spot size (mm)	Transmission (%)	measured Gain for 350 $\mu\text{m}$ pinhole	calculated Gain 350 $\mu\text{m}$ pinhole	calculated Gain 90 $\mu\text{m}$ pinhole	calculated Gain 10 $\mu\text{m}$ pinhole
6	0.09	36	78	81	645	911
8	0.08	49	96	110	933	1359
10	0.09	39	83	87	624	842
12	0.09	39	74	87	654	903
white	0.17	42	11	89	243	266

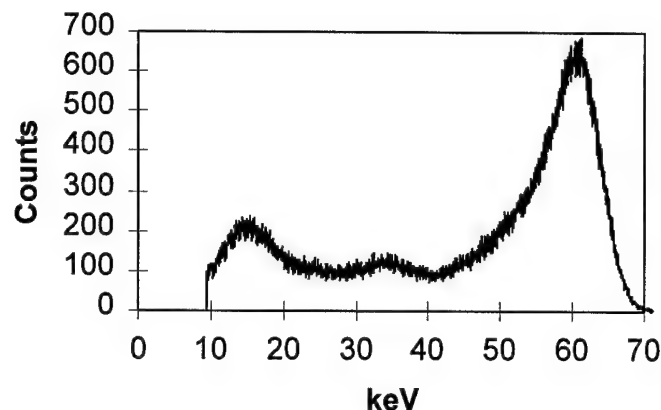


Figure 74. Spectrum from Am 241 taken with CZT single pixel detector.

### CZT Detector

Digirad, Inc. (formerly Aurora Technologies) was somewhat delayed by the late start date of their subcontract with the University at Albany due to contract formalities. However, a 1 cm long CZT array with 50  $\mu\text{m}$  pixels has been manufactured and tested. The interconnect options were researched and the decision was reached to employ indium bump technology to bond the detector to a sapphire or quartz interconnect board, which is then bonded to the readout chips. This approach eliminates the need to wirebond to the detector, and also reduces the pixel size and consequently the leakage current. The first prototype was built, which demonstrated some mechanical instability. It is believed this is fixable with epoxy. The detector is currently at Digirad under investigation.

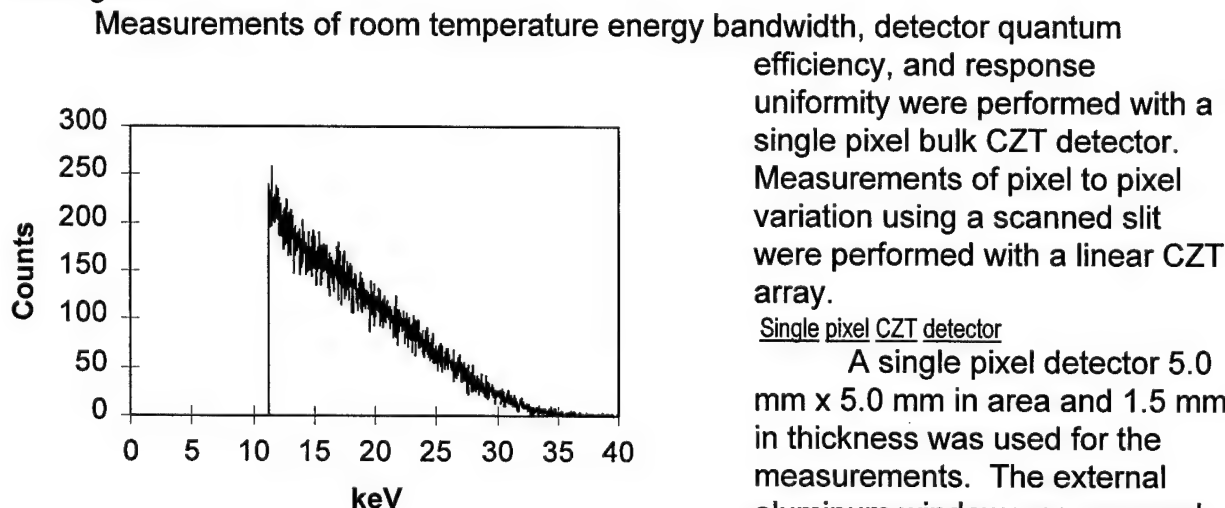


Figure 75. Spectrum of copper x-ray source, taken with single pixel CZT detector. The lower level discriminator was set at the lower end of the region of interest (ROI) marked in figure 5.

spot of the multifiber optic and one 20 mm closer to the optic, are shown in Figure 71. The derivatives of these scans are shown in Figure 73. The scan close to the focal spot has a smaller width than the scan far away from the focal spot. A plot of the width of the scan derivative as a function of distance from the multifiber optic is given in Figure 72. Resulting calculated and measured gains are shown in table 4

### **Direct Digital Detectors**

Measurements of room temperature energy bandwidth, detector quantum efficiency, and response uniformity were performed with a single pixel bulk CZT detector. Measurements of pixel to pixel variation using a scanned slit were performed with a linear CZT array.

#### Single pixel CZT detector

A single pixel detector 5.0 mm x 5.0 mm in area and 1.5 mm in thickness was used for the measurements. The external aluminum window was removed for the detector quantum efficiency measurement.

The spectrum produced by the CZT single pixel detector with

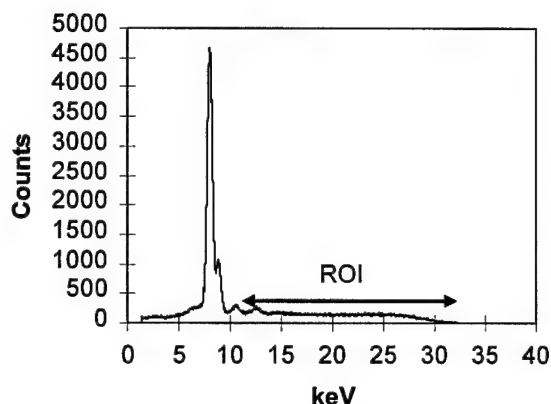


Figure 77. Spectrum of copper x-ray source, taken with HpGe detector. Lines at 10.5 and 12.6 keV are lead fluorescence from shielding. The region of interest (ROI) is marked.

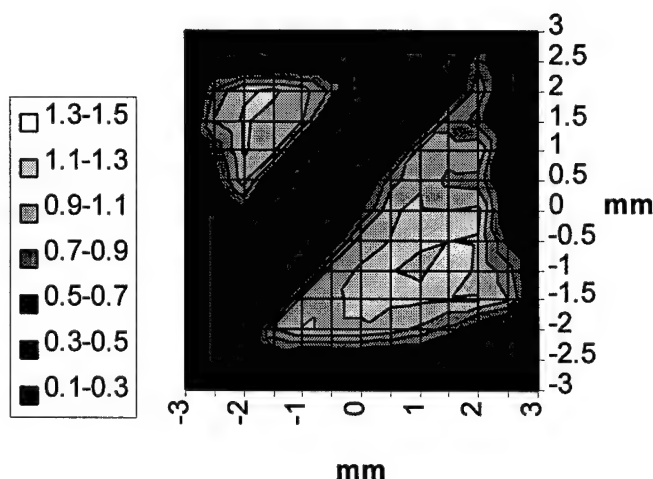


Figure 76. Pinhole scan of CZT single pixel with band of contact material.

a Am-241 radioactive source is shown in Figure 74. The spectrum was obtained with a Tennelec TC 241 linear preamplifier connected to a PCA-Multiport multichannel analyzer. The noise threshold at room temperature with this preamplifier is 10 keV. The FWHM of the Am 59.54 keV gamma is 9.5 keV at room temperature. The 17 and 24 keV lines of Am could not be resolved.

The detector quantum efficiency was measured in comparison to a high purity germanium (HpGe) detector with a 13 mm thick, 36 mm diameter crystal. For the HpGe detector, the efficiency was considered to be equal to unity in the energy range in which the experiment was performed. This detector was connected to the same linear amplifier and multichannel analyzer as the CZT detector. The distance between the source and the 100  $\mu\text{m}$  pinhole was 50 cm. The distance was chosen to maintain dead times less than 10%. The distance

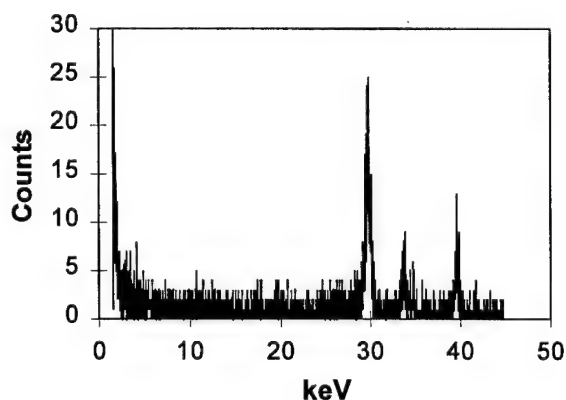


Figure 78. Spectrum from radioactive iodine taken with HpGe detector.

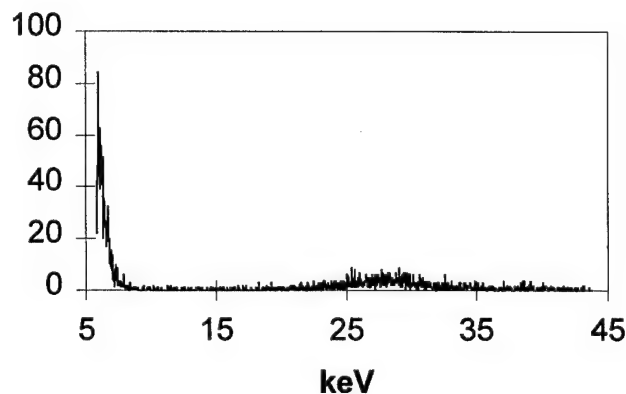


Figure 79. Spectrum from radioactive iodine taken with CZT detector



between the plane of the pinhole and the detectors was kept equal to 5 mm for both detectors, which was as small as possible given the HpGe detector geometry. The small separation reduces the effects of scattered or fluorescent radiation and ensures that the entire beam exiting the pinhole is intercepted by the detector. The HpGe detector was calibrated in energy using the Am gamma and the 5.9 keV line of Fe 55. The CZT detector was calibrated using the Am 59.54 keV line and a pulser set to equal and to half-height of this line.

Two different x-ray sources were used for this measurement. First was a copper x-ray tube with tube voltage of 30 kV, with the spectrum, obtained with the HpGe detector, shown in Figure 77. The resultant CZT spectrum for the same count time is shown in Figure 75. Interpretation of the results is complicated by two factors. First, the noise threshold, and therefore the lower level discriminator, is above the peak of the spectrum, so only the higher energy bremsstrahlung is recorded. Second, monoenergetic high energy photons, due to hole tailing effects, contribute to counts in a long Laurencian tail to lower energies, as seen for the Am gamma in Figure 74. Therefore counts due to photons with energy above the threshold are lost into lower energy channels. The detected quantum efficiency for this source, determined roughly as the ratio of integrated counts in the regions of interest shown in Figure 77 and Figure 75, was found to be 44 %. A similar measurement was performed for a radioactive iodine source, with the spectra shown in Figure 78 and Figure 79. The DQE for this source is 42%. An imaging detector, which counts events independent of energy, would be affected by the hole-tailing only to the extent that the ends of the tail are below the noise threshold.

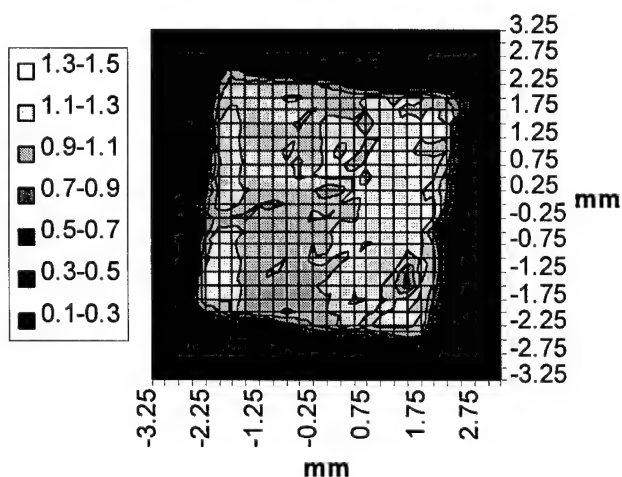


Figure 80. Pinhole scan of CZT single pixel.

Area uniformity measurements were performed on a bulk single pixel detector by scanning the active area of the detector with a 300  $\mu\text{m}$  pinhole. The result for the first detector tested is shown in Figure 76. The diagonal band is a strip of contact material normally unimportant for the operation of this detector in the infrared. The scan of a second detector, produced without this contact material, is shown in Figure 80. The average count rate in the 3.5 mm central area was normalized to unity. The variance in that region is 8%, 3% of which is due to Poisson statistics.

Some part of the variance (4%) is due to the external aluminum window. The semiconductor sensitivity is quite uniform over the entire pixel.

Linear array

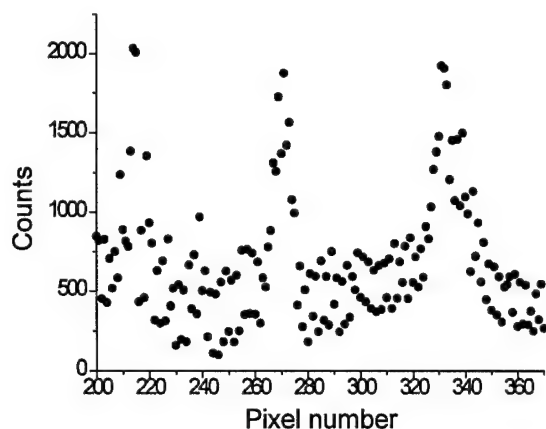


Figure 81. Image of slit taken with linear CZT array, without background subtraction.

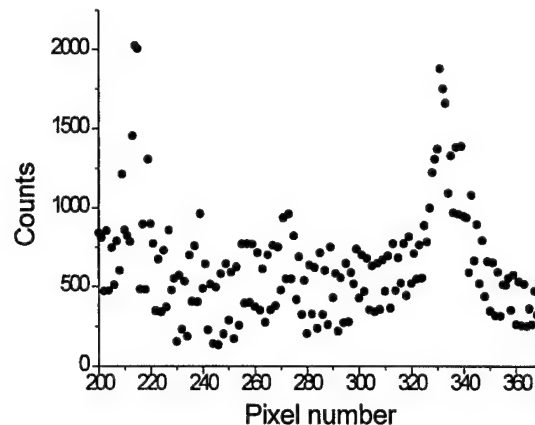


Figure 82. Background associated with image in figure 11.

The CZT linear array was attached to the read-out electronics by means of indium bump bonding technology. Measurements were performed only for the central pixels because mechanical stresses caused bonding failure for the end pixels. This will be corrected for future arrays with an addition of epoxy for mechanical adhesion. To check the uniformity of the response of the pixels to x-ray radiation, a 0.5 mm slit was placed between the detector and the copper x-ray source. The array was then mounted on a translation stage that allowed movement parallel to the plane of the slit. The result without background subtraction is shown in Figure 81. The background, counted for the same period without the source on, is shown in Figure 82. The background subtracted result is shown in Figure 84. Moving the detector to the left causes the peak to move to the right, as shown in Figure 83. Comparing the peak heights of six positions along the central part of the array gives a peak height variance of 25%. To establish that the variance was due to differences in pixel sensitivity, a full field measurement was taken with no slit. Dividing

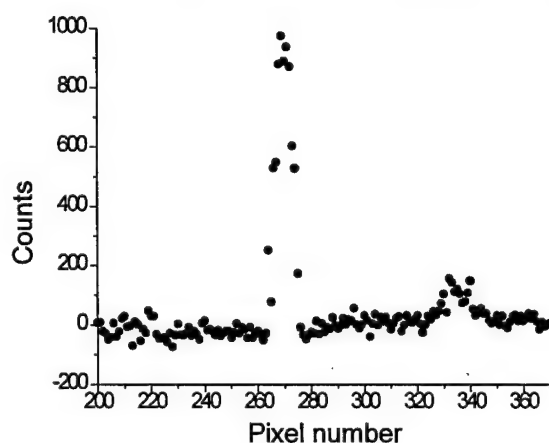


Figure 84. Slit image from Figure 86 with background from Figure 85 subtracted.

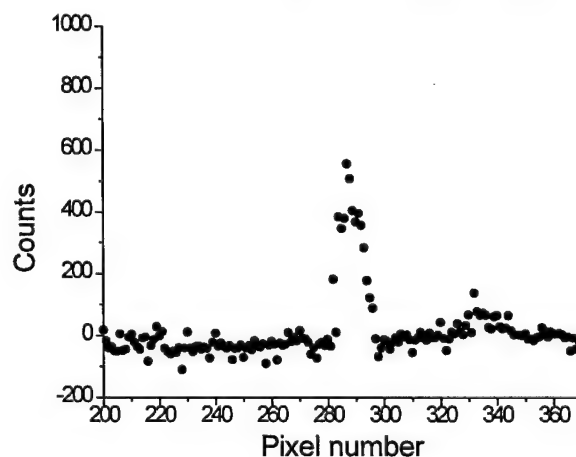


Figure 83. Background subtracted image of slit after moving detector to the left.

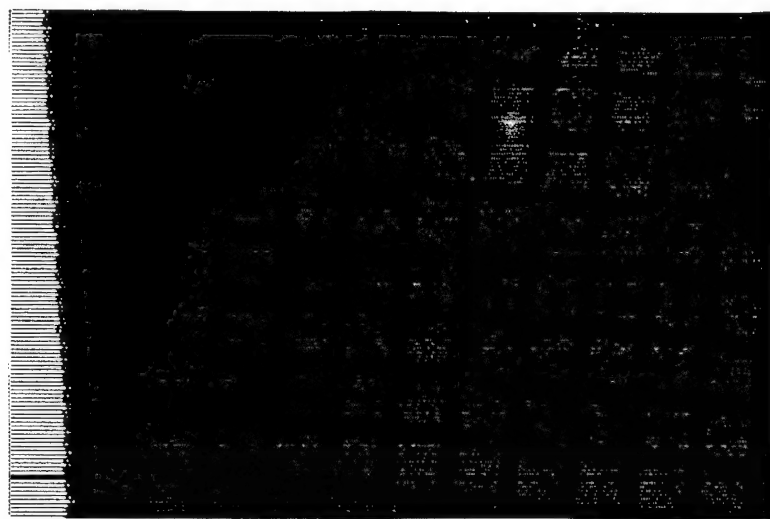


Figure 85. CID image of three grids. The largest has open spaces 560 microns wide and 300 micron wires. The smallest, unresolved at upper right, has 25 micron holes. The grid at center has 50 micron holes. The image was taken with magnification 1.02 onto the chip, which has 28  $\mu\text{m}$  pixels.

required for mammography.

#### CID Detector

Because of the questions in development of the CZT technology we have investigated a second technology, Charge Injection Devices (CID), as well. Like the more common CCD (Charge couple device) CID technology allows for rapid array imaging. Unlike the CCD, the CID is very radiation resistant. CID pixels can be read repeatedly and nondestructively, leading to very high dynamic range. CID well depths are also deeper than conventional CCDs, leading to a substantial reduction in blurring from high energy x-ray photons. The CID chips tested, which had 250x250 28  $\mu\text{m}$

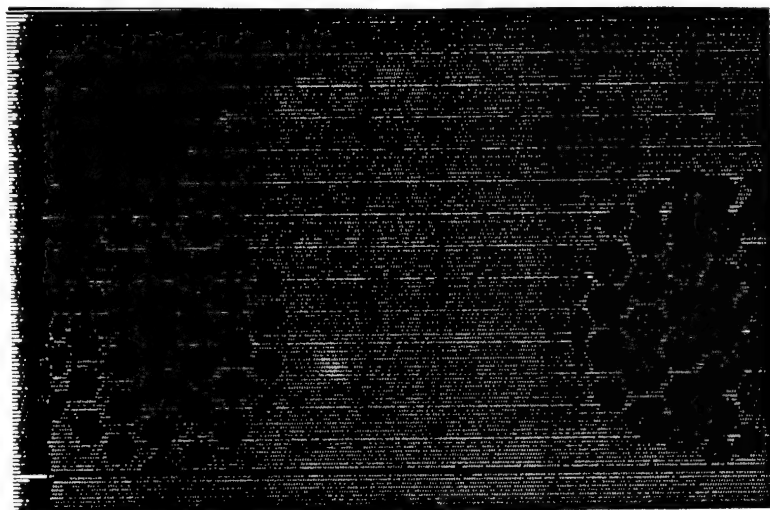


Figure 86. CID image of Lucite phantom shown in Figure 42.

the background subtracted slit image by the background subtracted full field image causes the two peak heights shown in Figure 84 and Figure 83 to agree within 6%.

Unfortunately, problems have developed in advancing this technology from linear to two dimensional arrays. Although only one-dimensional arrays were proposed in this project, it was recognized that the eventual outcome should be a 2D array. The current technology for 2D CZT arrays do not lend themselves to the small pixel sizes and relatively low x-ray energies (compared to nuclear gamma imaging)

pixels, were too thin to have good x-ray quantum efficiency without phosphor. However, large area chip technology is already available. The measured DQE for the device was 23% at 20 keV. At that energy only 29% of the photons are expected to be absorbed in the 8  $\mu\text{m}$  thick active region. Detector designs with thicker active areas will have larger DQEs. We are working with the manufacturer, CIDTec, to study the application of their

new x-ray dental imagers (with and without phosphor coatings) to mammography. Radiation damage testing measurements have been completed on prototype imagers. Initial testing of a prototype imager with phosphor resulted in mechanical stress damage which is being investigated. A second prototype for direct detection, without phosphor, will be delivered in the next few weeks.

## Conclusions

This is a high risk project with potentially very high gain. Any such project will have inevitable delays, frustrations and changes of direction. However, the delays and problems associated with this project have been fairly minor. Some manufacturing problems have occurred with both optics and detectors. These problems are being addressed by our studies of defect properties, and by changes being adopted in the manufacturing processes. Notwithstanding the problems, the optics tested have performed extremely well. A number of promising geometries are being studied: collimating optics with long and short focal lengths, with and without antiscatter optics, monolithic linear magnifying tapers, and monolithic focusing, demagnifying optics. The collimating optics have transmissions in excess of 30% at their design energies, with collection angles ranging from 8 to 12 degrees. Scatter rejection is very high from all the optics. The linear tapers resulted in nearly ideal contrast enhancements and simultaneously increase in MTF at all spatial frequencies. This will result in an improvement in resolution regardless the inherent spatial resolution of the detector. Just as important, if less spectacular, is the rapidly growing modeling capability. The modeling has lead to a real development of understanding of the nature of polycapillary defects, which is already leading to improvements in the manufacturing processes. Further, the increased confidence in the modeling allows future lens geometries to be effectively "tested" in simulation so that design parameters can be rapidly optimized.

Direct digital detector development is also promising. Two diverse detector technologies have been investigated. Both show considerable promise for providing simultaneous high resolution and high quantum efficiency. One dimensional "imaging" was demonstrated with the CZT linear array. The CZT detector has higher quantum efficiency without phosphor, but is more difficult to produce as a two-dimensional array with sufficiently low read-out noise and small enough pixels. However, this is largely a problem with the read-out electronics. As better electronics are becoming rapidly available, this technology becomes more attractive. The CID technology, while it would require some modification for phosphor free operation, is moving rapidly into the x-ray market, particularly in dental imaging. CID two dimensional array technology with small pixel sizes already exists. This is another promising new technology for mammography.

## References

- <sup>1</sup>Shern, F., Digital Mammography and Related Technologies: A Perspective from the national Cancer Institute, Radiology, 183(3), p.629-630, 1992.
- <sup>2</sup> M.A. Kumakhov, F.F. Komarov, "Multiple Reflection from Surface X-ray Optics," Physics Reports, **191**, (5): p. 289-350, 1990.
- <sup>3</sup> C.A. MacDonald, C.C. Abreu, S.S. Budkov, H. Chen, X. Fu, W.M. Gibson, Kardiawarman, A. Karnaukhov, V. Kovantsev, I. Ponomarev, B.K. Rath, J.B. Ullrich, M. Vartanian, Q.F. Xiao, "Quantitative Measurements of the Performance of Capillary X-ray Optics," Multilayer and Grazing Incidence X-ray/EUV Optics II, R.B. Hoover and A. Walker, eds., SPIE Proc. vol. 2011, 1993.
- <sup>4</sup> J.B. Ullrich, V. Kovantsev, C.A. MacDonald, "Measurements of Polycapillary X-ray Optics," Jour. Appl. Phys., **74** (10), to be published, Nov. 15, 1993.
- <sup>5</sup> C.A. MacDonald, "Applications and Measurements of Polycapillary X-Ray Optics," Journal of X-Ray Science and Technology, **6**, pp. 32-47, 1996..
- <sup>6</sup>C.C. Abreu, D.G. Kruger, C.A. MacDonald, C.A. Mistretta, W.W. Peppler, Q.F. Xiao, "Measurements of Capillary X-Ray Optics with Potential for Use in Mammographic Imaging," Medical Physics **22** (11), Pt. 1, pp. 1793-1801, November 1995.
- <sup>7</sup>A. G. Haus, in **Screen Film Mammography**, G.T. Barnes and G. Donald Frey, eds., Medical Physics Publishing, Madison, Wisconsin, 1991.
- <sup>8</sup>B.H. Hasegawa, The Physics of Medical X-ray Imaging, 2nd Ed., Medical Physics Publishing, Madison, Wisconsin, 1991.
- <sup>9</sup>Q.F. Xiao, I.Y. Ponomarev, A.I. Kolomitsev and J.C. Kimball, in R.B. Hoover, ed., **X-ray Detector Physics and Applications**, SPIE 1992.
- <sup>10</sup>B.L. Henke, E.M. Gullikson, and J.C. Davis, Atomic Data and Nuclear Data Tables, **54** (2), p. 181, 1993.
- <sup>11</sup>Lei Wang, B.K. Rath, W.M. Gibson, J.C. Kimball, C.A. MacDonald, "Measurement and Analysis of Capillary Optic Performance for Hard X rays," Jour. Appl. Phys., September 15, 1996.
- <sup>12</sup> Hui Wang, Lei Wang, W.M. Gibson, C.A. MacDonald, "Simulation Study of Polycapillary X-Ray Optics," in SPIE Vol 3444, July 1998.

- <sup>13</sup>Lei Wang and C.A. MacDonald, "Measurement of Capillary Optic Performance for Hard X rays," in R.B. Hoover and M.B. Williams, **X-ray and Ultraviolet Sensors and Applications**, SPIE vol. 2519, July 1995.
- <sup>14</sup>Lei Wang and C.A. MacDonald, "Measurement and analysis of capillary optic performance for hard x-rays", **Hard X-ray/Gamma-Ray and Neutron Optics, Sensors, and Applications**, R.B. Hoover, and F.P. Doty, eds., SPIE Proceedings Vol. 2859.
- <sup>15</sup> Lei Wang, C. A. MacDonald, and W. W. Peppler, Performance of Polycapillary Optics for Hard X-ray Imaging, submitted, Medical Physics.
- <sup>16</sup> B.K. Rath, W.M. Gibson, Lei Wang, B.E. Homan and C.A. MacDonald, "Measurement and Analysis of Radiation Effects in Polycapillary X-ray Optics," accepted, Journal of Applied Physics.
- <sup>17</sup> B.K. Rath, D.C. Aloisi, D.H. Bilderback, N. Gao, W.M. Gibson, F.A. Hofmann, B.E. Homan, C.J. Jezewski, I.L. Klotzko, J.M. Mitchell, S.M. Owens, J.B. Ullrich, Lei Wang, G.M. Wells, Q.F. Xiao, and C.A. MacDonald, Effects of intense x-ray radiation on polycapillary fiber performance, in R.B. Hoover and M.B. Williams, **X-Ray and Ultraviolet Sensors and Applications**, SPIE vol. 2519, July 1995.
- <sup>18</sup> C.C. Abreu and C.A. MacDonald, "Beam Collimation, Focusing, Filtering and Imaging with Polycapillary X-ray and Neutron Optics," invited review article, *Physica Medica*, vol. XIII, N.3, 1997, pp. 79-89.
- <sup>19</sup>D.G. Kruger, C.C. Abreu, W.W. Peppler, C.A. MacDonald, C.A. Mistretta, "Imaging Characteristics of X-ray Capillary Optics in Mammography," submitted, Medical Physics.
- <sup>20</sup> Qin-sheng Chen, Michel Defrise, and F. Deconinck, "Symmetric Phase-Only Matched Filtering of Fourier-Mellin Transforms for Image Registration and Recognition", *IEEE Transactions on Pattern Analysis and Machine Intelligence*, Vol. 16, No. 12, December, pp. 1156.
- <sup>21</sup> Hiroshi Fujita, et. al. "A Simple Method for Determining the Modulation Transfer Function in Digital Radiography", *IEEE Transaction on Medical Imaging*, Vol. 11, No. 1, pp. 34.
- <sup>22</sup> Ehsan Samei, Michael J. Flynn, David A. Reimann, "A Method for Measureing the Presampled MTF of Digital Radiographic Systems using an Edge Test Device", manuscript submitted to Medical Physics, 1996.

<sup>23</sup> John M. Boone and Seibert, "An analytical edge spread function model for computer fitting and subsequent calculation of the LSF and MTF", Medical Physics, Vol. 21, No. 10. October 1994., pp.1541